GeoScienceWorld
Lithosphere
Volume 2021, Article ID 5505884, 21 pages
https://doi.org/10.2113/2021/5505884

Lithosphere

Research Article

Submarine Basaltic Magmatism in the Subbetic Basin (Southern Spain): Insights into Melt-Weakening Processes during Mesozoic Continental Rifting

Juan Díaz-Alvarado,[1] **Antonio Pedrera**,[1] **Antonio Azor**,[2] **Jesús García-Senz**,[1] **José Alberto Díaz de Neira**,[1] **and Luis Roberto Rodríguez-Fernández**[1]

[1]*Instituto Geológico y Minero de España (IGME), Sevilla, Spain*
[2]*Departamento de Geodinámica, Universidad de Granada, Granada, Spain*

Correspondence should be addressed to Juan Díaz-Alvarado; juan.diaza@uda.cl

Received 20 July 2021; Accepted 4 October 2021; Published 23 October 2021

Academic Editor: Christoph Hauzenberger

Mantle-derived volcanic rocks from the Subbetic hyperextended basin in SE Spain provide new insights into the composition and mechanical behavior of the mantle during continental rifting. The present study describes a sequential restored cross-section along with geochemical characteristics of the basaltic rocks interbedded within the Mesozoic succession of the basin. Sedimentary stacking patterns of minibasins above the mobilized salt reflect the relationships with coeval basaltic volcanism. We recognize two type localities on the basis of volcanic facies, the presence of shallow intrusive bodies, and age of the associated sedimentary formations. The first type corresponds to subaqueous pillow-lava flows and subvolcanic sills and dikes associated with Lower Jurassic marly limestones and Middle Jurassic oolitic limestones. The Jurassic basalts present enriched MORB compositions with moderate La/Sm and low Sm/Yb ratios. Interestingly, a significant group of this Jurassic basaltic magmatism departs from the typical MORB-OIB array, showing deep Nb-Ta negative anomalies and high Th/Nb ratios. The second type comprises subaqueous lava flows, also including pillow-shaped basalts interlayered with hyaloclastite deposits and Upper Cretaceous clays, radiolarites, and marly limestones. The Cretaceous magmatism is characterized by highly enriched MORB compositions. Furthermore, the moderate Sm/Yb values and the positive correlation between LREE/HREE and Zr point to the involvement of deep (Grt-present) mantle sources in the origin of the Cretaceous basaltic melts. We interpret the Lower-Middle Jurassic calc-alkaline signal as due to the partial melting of recycled crustal rocks within the upper mantle, i.e., associated with remnants of pre-Mesozoic subducted slabs. These characteristics are similar to those described in Triassic basaltic rocks widespread throughout the External Zone of the Betic Cordillera. Mantle-derived basalts interlayered within the Lower Jurassic syn-rift deposits indicate that melting and deformation within the lithospheric mantle was initiated early during continental rifting. Accordingly, we suggest that Early to Middle Jurassic mantle melts promoted failure within the upper mantle, thus contributing to the inception of lithospheric-scale shear zones, which, in turn, controlled the evolution of this magma-poor hyperextended margin. Subsequently, rift evolution gave way to the activation of deeper melt sources in the mantle and an increase of the alkaline signature at the Cretaceous time.

1. Introduction

Magmatic and tectonic processes are intimately interrelated. Magmatism can contribute to dropping effective stresses, thus weakening the lithosphere and promoting rifting [1–3]. Conversely, continental rifts mostly nucleate on pre-existing orogenic features, which also represent preferred weakness zones (e.g., [4]). Although tectonic inheritance and melt-weakening processes are known to be key factors behind rifting, their connection and feedback are still poorly documented.

Preexistent crustal fabrics influence the strike of individual faults, thus triggering segmentation and oblique rifting (e.g., [5–9]). Nevertheless, numerical models show that

rifting mechanisms are primarily governed by the strength and thermal state of the lithospheric mantle (e.g., [10–16]). In conjunction with increasing geothermal gradient, inherited compositional heterogeneities within the upper mantle exert a primary control on the location of partial melting and the initiation of continental rifting [17–19]. Subsequently, positive feedback between melt production and extensional processes occurs. Stretching of the continental lithosphere reduces the overburden pressure, stimulating asthenospheric decompressional melting, while upward magma migration weakens the lithosphere (e.g., [14, 20–22]). Melt-weakening processes are crucial in the evolution of volcanic-rich rifted margins [18], but they have not been completely characterized in magma-poor ones. In the latter, very limited magmatic production occurs during drastic crustal stretching and exhumation of the lithospheric mantle [23, 24].

The geochemical variability of mantle-derived magmas associated with hyperextended margins reflects interplay between mantle heterogeneities and the depth at which the fertile mantle starts melting [19, 25–28]. MORB terminology in these continental settings is difficult to apply (e.g., [29]). The extent of crustal thinning and the presence of lithospheric-scale structures largely determine the so-called lid effect (lithosphere thickness) [30], which ultimately controls the volume and composition of basaltic magmas and their capacity to reach the upper crust in cold rift settings (e.g., [26, 31–33]).

In this paper, melt-weakening processes have been explored in the Subbetic hyperextended basin (Betic Cordillera, SE Spain), a failed branch of the Central Atlantic. Magmatic activity resulted in the emplacement of isolated subvolcanic/volcanic bodies within Upper Triassic evaporites and submarine lava flows interlayered between Lower Jurassic and Upper Cretaceous hemipelagic and pelagic sediments. We provide a new cross-section running along the main rift axis based on field and seismic reflection data. Sequential restoration allows us to describe the general basin architecture and the relationship between basaltic lava flows and sedimentary packages. Our new geochemical results from the volcanic record in this Mesozoic basin have been analyzed and compared with data from other rift basins in order to unravel the early rifting processes and their subsequent evolution. Furthermore, we discuss the role of inherited crustal fabrics in the inception of oblique rifting at this region of the Iberian plate.

2. Geological Setting

The Betic Cordillera (SE Spain) is located in a region that underwent Variscan collision at the late Paleozoic time and subsequent lithosphere stretching during two distinct rifting episodes at Permian-Triassic and Early Jurassic-Early Cretaceous times (Figure 1). The geology of the Variscan belt in Southern Iberia encloses three main NW-SE trending tectonic zones that represents continental pieces separated by complex shear zones attesting to subduction and exhumation processes (e.g., [34–37]). These continental fragments are characterized by pervasive fabrics formed during the Variscan collision, important Carboniferous basins, and large igneous bodies (e.g., [38–40]). Some of these pre-Mesozoic structures constitute weakness zones prone to be reactivated under extension, thus providing a template for the formation of a Mesozoic rifted margin, subsequently inverted at Alpine times (Figure 1(a)).

The Betic Cordillera forms, together with the Rif Mountains in NW Morocco, the southwestern termination of the Alpine orogen, formed as a result of the complex collision between the Eurasian and African plates (Figure 1(b)) (e.g., [41–44]). The central part of the Betic Cordillera is subdivided from north to south into the External and Internal Zones (e.g., [45]). The Internal Zone is composed of three tectonic complexes referred to as Maláguide, Alpujárride, and Nevado-Filábride, comprising Paleozoic and Mesozoic rocks, variably affected by ductile deformation and metamorphism (e.g., [46, 47]). The lower complex is the Nevado-Filábride one, constituted by rocks of the South Iberian Margin subducted below the other two complexes [48–51]. Metabasalts and serpentinized ultramafic rocks having recorded early Miocene (Burdigalian) HP metamorphism are found at the structural top of the Nevado-Filábride Complex, close to the contact with the overlying Alpujárride Complex (e.g., [52]). This primarily subduction-related contact was reactivated later during the middle Miocene as a low-angle ductile-brittle extensional shear zone [53, 54].

The External Zone of the Betic Cordillera is organized as a NW-directed fold-and-thrust belt that resulted from the thin-skinned tectonic inversion of Mesozoic salt-floored deposits unconformably overlying the South Iberian rifted margin (Figure 1(b)) (e.g., [44, 55–60]). The inversion of the Mesozoic sedimentary cover was coeval to the subduction of the South Iberian continental lithosphere [44, 48]. Based on lithostratigraphic differences of the Lower Jurassic-Upper Cretaceous syn-rift successions, the External Zone is subdivided into three structural units with paleogeographic meaning, referred to as Prebetic, Intermediate, and Subbetic (e.g., [61, 62]).

2.1. The Subbetic Basin. The Subbetic units were deposited over the South Iberian passive margin, which was laterally connected with an oceanic domain in the Late Jurassic. According to this interpretation, the Subbetic units represent a gateway floored by oceanic crust that connected the North Atlantic with the Tethyan oceanic domains to the east (e.g., [41, 63–67]). However, recent reconstructions propose that oblique continental rifting failed before lithospheric breakup [44]. According to this kinematic model, the Betic realm encloses five rift domains segmented by WNW-ESE transfer faults, with oceanic spreading restricted to the western domain (distal part of the Algarve Basin and Betic Flysch Trough). Likewise, the central-eastern portion of the Subbetic Basin recorded hyperextension with possible exhumation of the continental mantle (Figure 1(c)).

The Subbetic Basin comprises three main domains (e.g., [61]) highly influenced by the presence of Upper Triassic salt- and clay-bearing rocks, which promoted complete decoupling between basement and cover (Figures 1 and 2). The interaction between salt/clay rocks and ENE-WSW

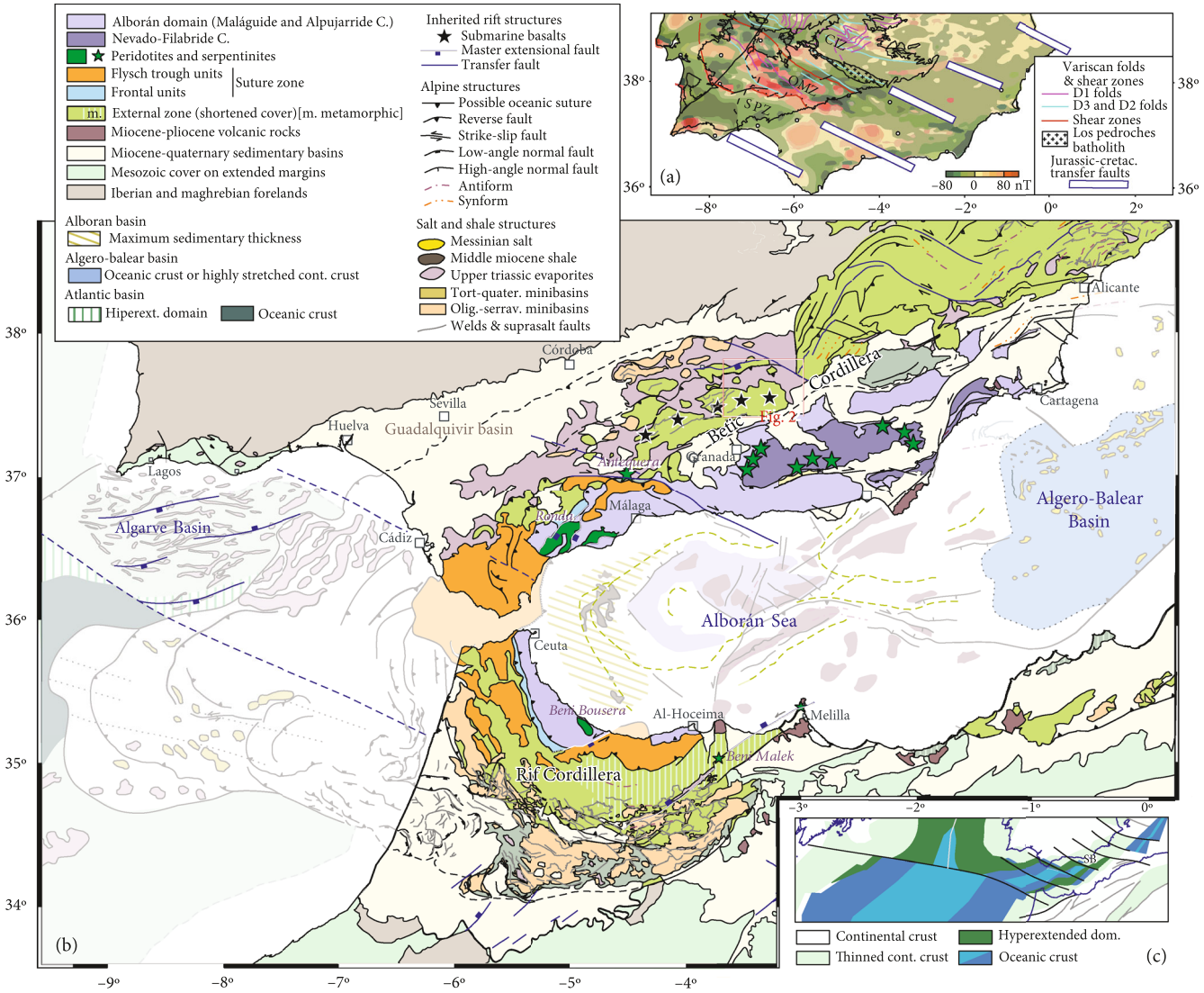

FIGURE 1: (a) Simplified geology of the Variscan belt in Southern Iberia showing the axial traces of the folds and the main shear zones [114] plotted over the aeromagnetic anomaly map [102]. Note that the WNW-ESE trend of the Variscan structures fits the elongated magnetic dipoles that extend beneath the Guadalquivir foreland basin and the Jurassic-Early Cretaceous transfer faults [44]. SPZ: South Portuguese Zone; OMZ: Ossa-Morena Zone; CIZ: Central Iberian Zone. (b) Simplified tectonic map of the Betic-Rif Cordillera and adjacent continental and oceanic margins indicating the inherited Mesozoic rift structures (modified from [44]). The location of Figure 2 is indicated as a box. (c) Kinematic reconstruction of the Central North-Atlantic and propagation towards the Betic Domain at 126 Ma (lowermost Aptian) (after [44]). The location of the Subbetic Basin (SB) is marked.

rift-parallel faulting controlled the thickness and facies distribution of overlying minibasins [44]. The central portion of the Subbetic Basin is characterized by a northern sector with thick minibasins (Prebetic and Intermediate Units), a central sector with condensed pelagic units over inflated salt (External Subbetic units), and a southern sector with primary minibasins featuring interbedded submarine volcanic rocks overlying hyperextended crust (Median and Internal Subbetic). Magmatism along this southern sector triggered a protooceanic spreading center, but extension stopped before the accretion of unambiguous oceanic crust (Figure 1).

The inversion of the Mesozoic Subbetic Basin started at the Paleogene time. The Alpine shortening gave way to squeezed salt walls, thrust welds, and allochthonous salt canopies [44, 57]. Additional shortening formed two main thrust sheets: the upper one encloses minibasins originally placed in the southern part of the basin (Internal, Median, and External Subbetic), which were displaced northwards, overthrusting minibasins of the northern side; the lower thrust sheet transported all these structures towards the foreland. Eocene-Miocene syn-orogenic deposits filled the wedge-top and the Guadalquivir foreland basin.

3. Architecture of the Subbetic Basin and Occurrence of Volcanic Activity

A detailed cross-section was constructed based on field and seismic reflection data (section 85-G-05; Figure 2) to

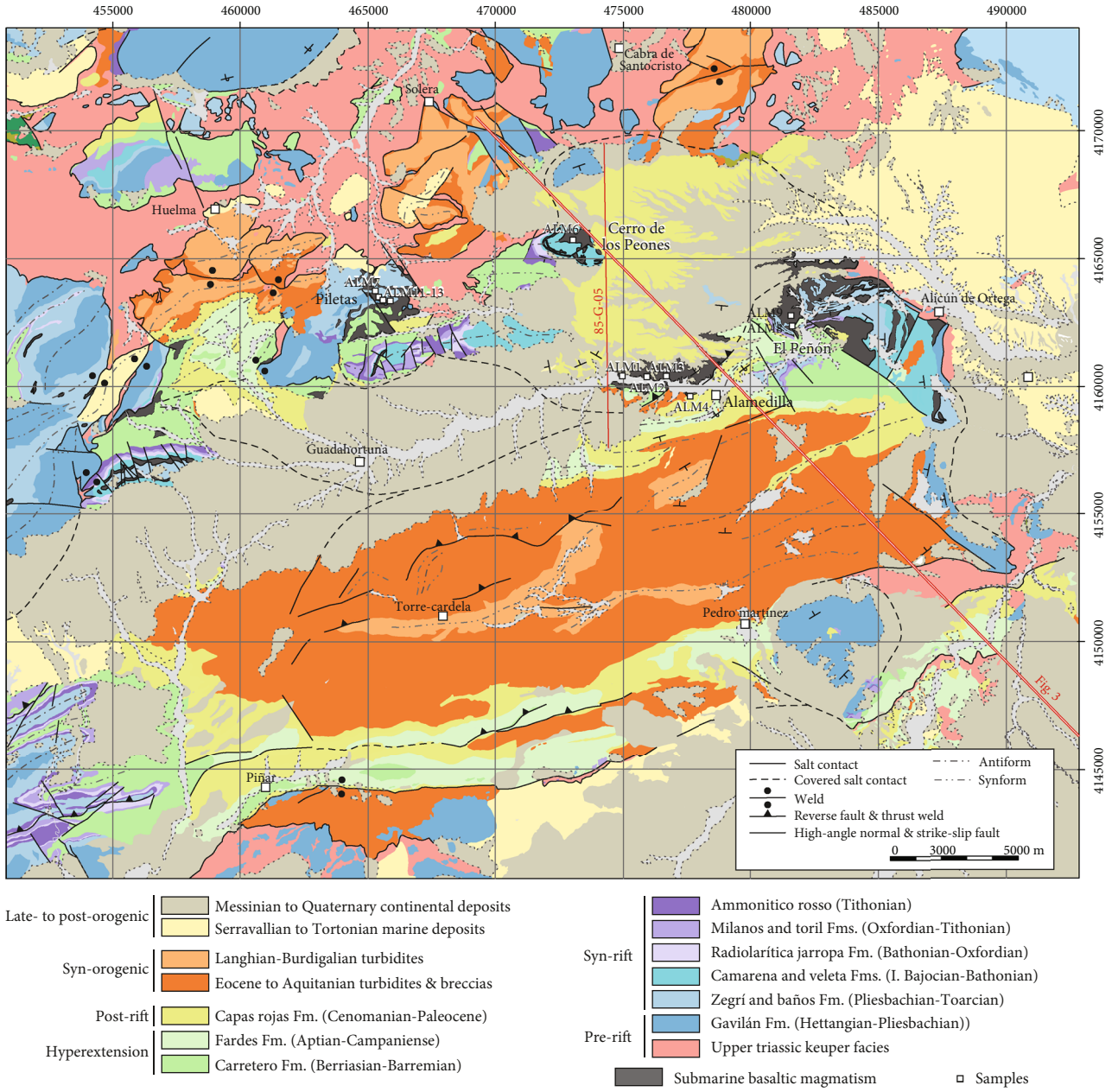

Figure 2: Geological map of the studied sector within the Betic External Zone (inverted Subbetic Basin), showing the location of the studied samples, the cross-section in Figure 3, and the seismic line used in the interpretation.

constrain the structure of the Subbetic Basin in the sector where the volcanic rocks were sampled. The studied basaltic rocks were deposited in two primary minibasins of the upper thrust sheet (Figures 1 and 2). These rocks are interlayered within Lower Jurassic to Upper Cretaceous sediments. The restored cross-section reveals the architecture of the minibasins, providing a geometrical framework for the lithostratigraphic and chronostratigraphic descriptions, which, in turn, enable precise spatial and temporal locations of the volcanic occurrences within the minibasins (Figures 3 and 4).

The accommodation space in these minibasins was created by expulsion of the underlying Upper Triassic evaporitic unit (Figures 3 and 4). A continuous thin carbonate platform (Gavilán Fm.) covered this basal unit of the basin during the Early Jurassic (e.g., [68]). Immediately above, the Toarcian Zegrí Fm. contains marl-limestone intercalations in the lower part and nodular marly limestones in the upper part. This formation represents the onset of the syn-rift stage and records the first appearance of interlayered basalts. Shallow-water oolitic limestones (Camarena Fm.) formed narrow platforms on the boundaries of the minibasin coevally to profuse flood-basalt lava deposits at Bajocian-Bathonian times. Some of these carbonate platforms covered the submarine volcanic edifices (e.g., [68]). Carbonate deposits evolved into radiolaritic marls and radiolarites of the Bathonian-Oxfordian Jarropa Fm., probably deposited at moderate water depth [69]. The overlying Milanos Fm. is constituted by marly limestones with chert,

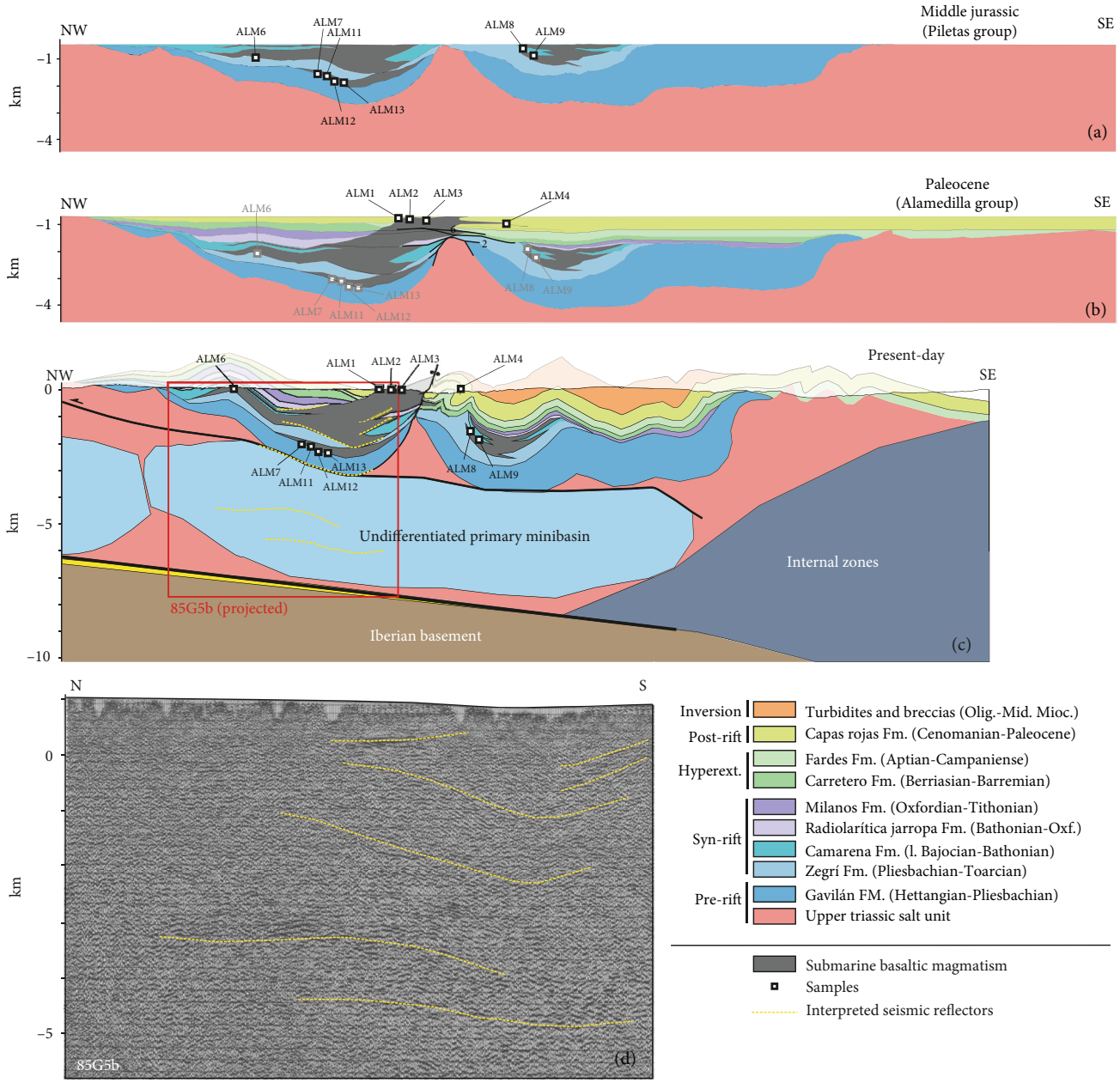

Figure 3: (a–c) Geologic cross-sections and sequential restoration along rift axes to denote interaction between the basaltic volcanism and the sedimentary packages sinking into underlying salt. The location of the studied samples is marked. (d) Depth-converted 85G5b seismic profile with the main interpreted reflector. Seismic data are projected in the cross-section of (c).

in which calcarenitic and calcisiltitic levels with hummocky cross-stratification were interpreted as storm layers in an outer marine platform [70, 71]. Slumped limestone-marl alternations also including breccias with redeposited pebbles from the underlying formations (Carretero Fm.) record instabilities within the boundaries of the minibasin during the Berriasian-Hauterivian (e.g., [72]). Green clays and radiolarites with intercalations of carbonate and conglomerates were deposited in the central and southern part of the minibasin at Aptian-Albian times (Fardes Fm.) [73]. The Cenomanian to Paleocene postrift sequence is characterized by white and pink marly limestones (Capas Rojas Fm.); they include pelagic microfossils and record an overall transgressive evolution. Voluminous lava-flow deposits are interlayered between the Fardes and Capas Rojas formations.

4. Field Relations and Characteristics of the Volcanic Deposits

We distinguish two type localities according to volcanic facies, presence of shallow intrusive bodies, and age of the associated sedimentary formations.

4.1. Alamedilla. The Alamedilla outcrops (Figures 2–4) show thick, pillowed, submarine lava flows, hyaloclastites, and

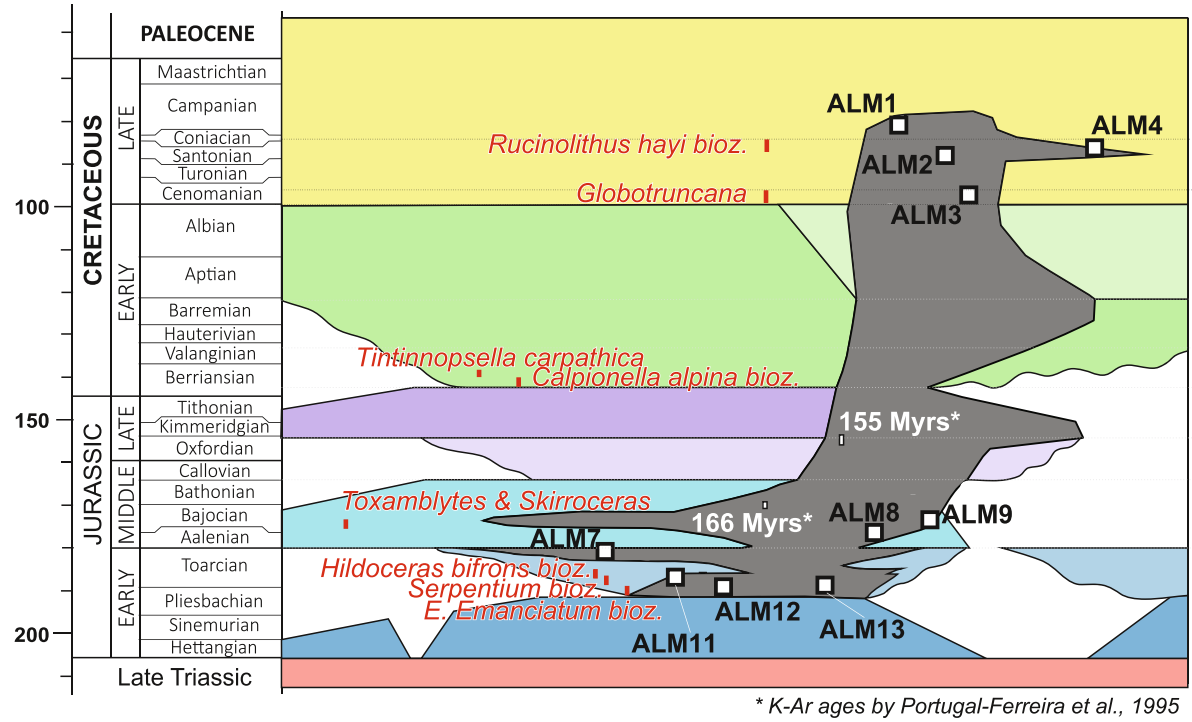

Figure 4: Wheeler diagram representing stratigraphic succession, volcanic occurrences, and studied samples, in a time-space framework. Biostratigraphic zones and absolute ages are included.

basaltic pillows embedded in fine-grained sediments. Tectonic deformation does not significantly affect the original depositional contacts in this area. The restored cross-section reveals an asymmetrical stacking pattern of the basaltic lava lobes, progressively onlapping southwards (Figures 3 and 4). Laterally, rounded fragments of basaltic lavas were observed within Santonian marls and limestones from the Capas Rojas Fm. [74].

Subaqueous extrusive volcanism consists of 5-8 m thick lava flows interlayered with hyaloclastite deposits and carbonate-rich mud sediments that embed numerous pillow-shaped basalts (Figure 5(a)). The thicker lava flows exhibit a wide variety of pillow shapes. Spherical, flattened, or tabular pillows are frequently interconnected by lobes and tubes, presenting 1-3 cm thick glassy quenched rinds (Figure 5(b)). The irregular depositional contacts between volcanic deposits and the long axes of pillow lavas indicate seafloor paleoslopes. The more elongated the shapes, the more steeply inclined the slopes and/or thicker volcanic columns (Figure 5(c)). Downslope in pillow accumulation areas, hot interiors promoted ductile behavior of chilled margins and close packing of former spherical pillows. A thin layer of carbonate-rich mud exposes sharp, irregular pillow rinds (Figure 5(d)).

4.2. Piletas. The Piletas area represents a basaltic domain where both subaqueous extrusive deposits and subvolcanic sills and dikes are associated with Lower Jurassic marly limestones (Zegrí Fm.) and Middle Jurassic oolitic limestones (Camarena Fm.). Besides the samples located in the Piletas locality, an additional sample was collected in the Cerro de los Peones (Figure 2). Middle Jurassic basalts were also sampled in the El Peñón area (Figures 2 and 3). Lava flows (ALM-8) and pillowed deposits (ALM-9) dominate this area with intermediate characteristics between the Lower Jurassic and the Cretaceous magmatism.

Pillowed lava flows in Piletas-type areas are similar to those described in the Alamedilla area (Figures 5(a)–5(d)). Furthermore, subvolcanic intrusives pervade partially consolidated, likely wet, carbonate-rich sediments and hyaloclastites. An anastomosing network of sill-like shallow intrusions presents variable thickness (between 2 m and a few centimeters) due to the lateral growth of dome-like structures (Figure 5(e)). During rapid cooling, polygonal (mainly hexagonal) fractures were generated, and sills finally acquire a hive-shaped structure. Basaltic fragments are limited by calcite veins with comb-layering textures due to the infiltration of $CaCO_3$-rich fluids through the quenching fractures (Figure 5(f)).

5. Textural Features and Geochemistry of Basaltic Rocks

5.1. Analytical Methods. Approximately 5 kg of basaltic rock per sample were collected. Subsequently, they were crushed and milled to a fine powder for whole-rock geochemistry. Major elements and Zr were determined by X-ray fluorescence (XRF) at the Centro de Instrumentación Científica

Figure 5: Representative studied outcrops of the subaqueous extrusive volcanism and subvolcanic facies of the Subbetic Basin. (a) Pillow-rich fine-grained sediment overlying a pillowed basaltic flow. (b) Varied morphologies of a subaqueous, pillowed lava flow. (c) Stretched pillows embedded in a carbonate-rich muddy sediment. Dark pillow margins exposing glassy quenched rinds. Long axes of the ellipsoidal pillows indicate the slope of the paleorelief. (d) Closely packed, formerly spherical pillow lavas. (e) Basaltic sills in the Piletas area with a characteristic "hive" arrangement. (f) Polygonal fractures originated during the rapid cooling of a basaltic sill intruding wet sediments. 1: large spherical pillow having concentric and radial fractures and a thin quenched rind; 2: lava tube interconnecting two spherical pillows; 3: elongated or flattened pillow; 4: three-dimensional view of the basaltic flow showing pillow lobes and interconnected tubes that allowed for the advance of viscous lava; 5: trapdoor structure; 6: lobulated "hot" contacts between accumulated pillows.

(CIC) of the University of Granada (Spain). Precision for major elements is better than 1% relative. Trace elements, except Zr, were analyzed by inductively coupled plasma mass spectrometry (ICP-MS), likewise at the CIC of the University of Granada, following the standard procedures described by Baedecker [75]. Analysis of trace elements was carried out according to the method described by Bea et al. [76]; the precision was approximately 2% and 5% on concentrations of 50 and 5 ppm, respectively.

5.2. Sampling Strategy and Comparative Data. With the aim of studying the geochemical characteristics of the basaltic magmatism in the Subbetic domain, 11 samples of pillow lavas and subvolcanic sills were analyzed. Major and trace element analytical results are presented in Table 1. Trace element contents (see Supplementary material (available here)) were furthermore projected in several geochemical diagrams in order to classify the basaltic magmatism associated with rifting and hyperextension of the South Iberian Mesozoic paleomargin, as well as to delve into the nature and conditions at the mantle sources that were activated during the evolution of the extensional process. According to the restored cross-section and the lateral relationship with sedimentary formations, we assign a Cenomanian-Santonian age to the samples obtained from the Alamedilla area and a Toarcian-Bathonian age to the Piletas and Cerro de los Peones volcanic/subvolcanic rocks (compiled as Piletas samples from now on). The youngest basalts of the Piletas area underlie the volcanic deposits sampled in the El Peñón area (Figures 3 and 4).

Few studies have focused on the geochemistry of basaltic magmatism in the Betic Cordillera. We selected analytical results available in the literature to complement our study. Traditionally, the term "ophite" has been used when referring to the mainly subvolcanic Triassic to Jurassic basaltic magmatism in the Subbetic region [77, 78]. Our geochemical projections include the averaged compositions of two groups of ophites: post-Triassic Group 1 and Upper Triassic Group 2 compiled by Morata [77]. According to this author, the two groups share the same mantle sources, with slight geochemical differences owing to higher crustal contamination in the late Triassic basalts (Group 2), generated during the initial rifting stages. Additionally, we consider recent geochemical results obtained in the Norian-Rhaetian volcanic rocks of the Zamoranos Fm. exposed in the Betic External Zone [79]. We moreover projected the Mesozoic metabasalts of the Nevado-Filábride Complex, which have been interpreted either as a mafic-ultramafic association representing a dismembered ophiolitic sequence [78, 80] or as subcontinental mantle-derived rocks formed during continental rifting (e.g., [81]). As general comparative data, the Zagros ophiolites were chosen; they are referenced in numerous geochemical studies, including MORB, OIB, and arc-related basalts, among others [27, 82, 83].

5.3. Petrographic Characteristics. The inner parts of the pillowed basaltic lavas are constituted by euhedral to subhedral Ol microphenocrysts included in a Pl+Px microcrystalline matrix (mineral abbreviations after [84]). A partially devitrified glass is present in interstitial positions (Figures 6(a) and 6(b)). Skeletal Pl laths are grouped into sheaf-like or radiated clusters. Cpx shows anhedral and feathery textures in the interstices between Pl clusters and Ol phenocrysts (Figure 6(a)). For the more vitreous quenched margins, only skeletal Ol phenocrysts are preserved as recognizable minerals, enclosed in a glassy (nondevitrified) groundmass. Similar textures were observed in the hyaloclastite deposits interlayered with the subaqueous lava flows of the Alamedilla area (Figure 6(c)). Irregular vitreous lava fragments are embedded in carbonate-rich sediment (Figure 6(d)).

Regarding subvolcanic sills and dikes, shallower basaltic intrusions (Figures 5(e) and 5(f)) show porphyritic microcrystalline textures, similar to those described in lava flows (Figures 6(a) and 6(b)). In the Piletas area, some deeper intrusions present fine- to medium-grained phaneritic textures. Gabbroic rocks show large Ol phenocrysts (0.5 to 1 cm in size) enclosed in a Pl+Px ophitic to subophitic matrix (Figure 6(e)). Ol crystals are serpentinized and present partially embayed surfaces in contact with Cpx (Figure 6(f)). Both Ol phenocrysts and tabular Pl crystals are randomly oriented and enclosed in large Px crystals.

To sum up, aphanitic, microcrystalline, and fine-grained basaltic rocks of the Alamedilla- and Piletas-type areas present similar mineralogical compositions. Alteration processes affected primary mineral assemblages, and chlorite, serpentine, and sericite, among other secondary minerals, were identified in the Subbetic samples. Secondary processes likely resulted in the high LOI contents analyzed in some samples. Infilled amygdulitic vesicles (chlorite, calcite, and analcime) were excluded during the sample preparation.

5.4. Geochemical Results. SiO_2 and alkali contents serve to classify most of the studied samples as basalts ($SiO_2 < 52$ wt% and total alkali > 3 wt% on an anhydrous base). Only the subvolcanic rock ALM-12, which presents the highest MgO and the lowest alkali contents, can be classified as a picrite or komatiite [85]. Except for the ALM-13 sample, the Piletas basalts show higher #Mg values (0.64-0.73) and FeO and MgO contents than the Alamedilla samples (#Mg = 0.35 – 0.56). To the contrary, the Alamedilla lavas present higher TiO_2, CaO, alkali, and P_2O_5 contents (Table 1). #Mg and Fe-Mg oxides show a positive correlation for the Alamedilla and Piletas groups of samples. Furthermore, CaO, TiO_2, and alkali contents increase as the #Mg decreases. These characteristics point to early, short-range Ol±Pl±Px fractionation in the basaltic melts, which can also be inferred from the presence of Ol phenocrysts in the glassy lavas and microcrystalline subvolcanic basalts (Figure 6).

Major element results should be analyzed with some caution due to the likely seafloor and/or hydrothermal alteration superimposed on the pristine geochemical characteristics of basalts. Actually, wide variations are observed in Ca, Fe, and Mg contents, with differences of up to 6-8 wt% for major oxides (Table 1). Element mobility entails an important limitation when analyzing the geochemical compositions of basaltic rocks affected by alteration and/or hydrothermalism. Nevertheless, a good number of incompatible trace elements—such as transition metals, REE

Table 1: Whole-rock major and trace element compositions of the studied basaltic rocks in the Subbetic domain.

Locality	Alamedilla				Cerro de los Peones		Piletas			El Peñón	
Sample	ALM-1	ALM-2	ALM-3	ALM-4	ALM-6	ALM-7	ALM-11	ALM-12	ALM-13	ALM-8	ALM-9
Rock type (wt%)	Pillow lava	Pillow lava	Pillow lava	Pillow lava	Pillow lava	Subvolcanic rock	Subvolcanic rock	Gabbro	Subvolcanic rock	Pillow lava	Pillow lava
SiO_2	44.87	43.37	47.12	45.27	44.92	46.05	45.32	41.22	45.54	39.52	50.00
TiO_2	1.92	1.70	1.52	1.81	1.78	1.00	0.86	0.66	1.48	1.70	1.71
Al_2O_3	16.28	15.35	15.94	15.94	17.27	17.65	16.58	10.14	15.51	16.46	16.42
FeOt	6.92	10.19	11.82	8.67	8.76	9.19	9.82	13.47	8.21	6.87	7.54
MgO	5.01	4.54	6.11	2.58	8.92	10.75	11.56	20.68	3.82	4.23	5.98
MnO	0.15	0.10	0.14	0.05	0.06	0.14	0.14	0.18	0.11	0.16	0.04
CaO	8.27	8.69	8.32	10.16	6.69	5.77	4.99	3.55	12.78	14.55	4.40
Na_2O	1.68	1.98	3.06	2.37	1.75	2.94	3.39	1.25	2.74	2.13	2.47
K_2O	3.80	3.52	1.02	3.20	0.82	0.34	0.22	0.33	2.09	2.13	5.30
P_2O_5	0.40	0.32	0.28	0.38	0.22	0.15	0.14	0.11	0.25	0.23	0.29
LOI	9.27	8.79	2.64	8.63	7.95	4.98	5.95	6.99	6.35	11.29	4.74
Total (ppm)	98.57	98.55	97.97	99.06	99.14	98.96	98.97	98.58	98.9	99.27	98.89
Li	129	92.2	24.3	49.1	92.6	27.0	26.3	22.7	32.5	37.6	60.3
Sc	19.4	19.9	22.4	21.8	28.4	18.3	20.1	16.3	24.0	29.0	18.2
V	143	142	146	105	180	124	147	112	162	171	170
Cr	186	182	209	213	217	258	323	315	249	225	233
Co	79.4	48.7	43.0	41.7	65.3	44.2	55.6	99.2	36.7	54.5	27.2
Ni	233	135	143	106	105	63.1	90.6	511	107	203	16.5
Zn	211	136	92	227	85.3	73.0	96.3	83.7	76.9	95.0	45.5
Ga	16.8	17.3	17.4	16.3	17.5	15.3	14.2	9.3	16.0	16.2	18.8
Rb	43.2	81.0	22.2	61.7	6.45	8.80	8.12	15.1	27.1	25.5	19.2
Sr	245	394	332	485	134	184	164	93	268	322	260
Y	17.7	17.6	18.7	19.2	17.2	14.4	12.8	10.0	17.2	15.5	17.9
Zr	158	139	122	154	111	84.9	75.0	50.3	115	113	145
Nb	28.1	25.7	19.0	19.9	8.90	7.63	6.70	5.14	14.9	11.1	19.2
Cs	1.47	7.25	1.19	3.97	0.34	1.97	2.47	1.52	0.87	0.87	0.41
Ba	274	163	92.2	197	46.1	85.0	61.9	42.9	110	75.8	130
La	14.6	14.0	11.6	15.1	5.81	8.15	6.02	4.74	9.48	13.5	13.0
Ce	31.7	30.7	25.7	31.9	15.1	18.9	15.0	11.5	21.7	17.8	33.6
Pr	3.68	3.45	2.94	3.73	1.72	2.00	1.55	1.11	2.49	2.04	3.48
Nd	15.3	14.4	12.5	15.7	8.00	8.29	6.67	4.63	10.9	9.08	14.6
Sm	3.44	3.33	3.04	3.68	2.37	1.97	1.62	1.07	2.77	2.37	3.51
Eu	0.84	0.78	0.95	0.67	0.50	0.62	0.28	0.73	1.39	0.84	0.39
Gd	3.33	3.22	3.12	3.68	2.64	2.07	1.78	1.24	2.89	2.47	3.36

Table 1: Continued.

Locality	Alamedilla				Cerro de los Peones		Piletas			El Peñón	
Sample	ALM-1	ALM-2	ALM-3	ALM-4	ALM-6	ALM-7	ALM-11	ALM-12	ALM-13	ALM-8	ALM-9
Rock type (wt%)	Pillow lava	Pillow lava	Pillow lava	Pillow lava	Pillow lava	Subvolcanic rock	Subvolcanic rock	Gabbro	Subvolcanic rock	Pillow lava	Pillow lava
Tb	0.56	0.55	0.55	0.48	0.51	0.36	0.23	0.20	0.50	0.45	0.60
Dy	3.24	3.21	3.34	3.50	3.12	2.36	2.07	1.49	3.06	2.76	3.45
Ho	0.63	0.63	0.67	0.68	0.62	0.51	0.45	0.35	0.61	0.56	0.65
Er	1.67	1.68	1.78	1.75	1.69	1.40	1.26	1.01	1.64	1.54	1.77
Tm	0.24	0.25	0.26	0.25	0.25	0.21	0.19	0.16	0.24	0.23	0.26
Yb	1.45	1.50	1.59	1.50	1.50	1.30	1.20	0.97	1.47	1.40	1.56
Lu	0.21	0.22	0.23	0.22	0.21	0.19	0.18	0.14	0.21	0.20	0.22
Hf	3.26	3.15	2.79	3.14	2.25	1.81	1.46	0.89	2.42	2.45	3.41
Ta	2.30	2.04	1.37	1.33	0.34	0.24	0.15	0.05	1.02	0.55	1.30
Pb	46.9	2.54	2.60	3.94	0.83	4.86	2.27	1.81	1.75	0.91	1.30
Th	3.08	2.90	2.64	3.06	1.92	2.49	2.26	1.94	2.33	1.96	3.57
U	0.86	0.70	0.58	0.62	0.28	0.41	0.35	0.25	0.40	0.68	0.91

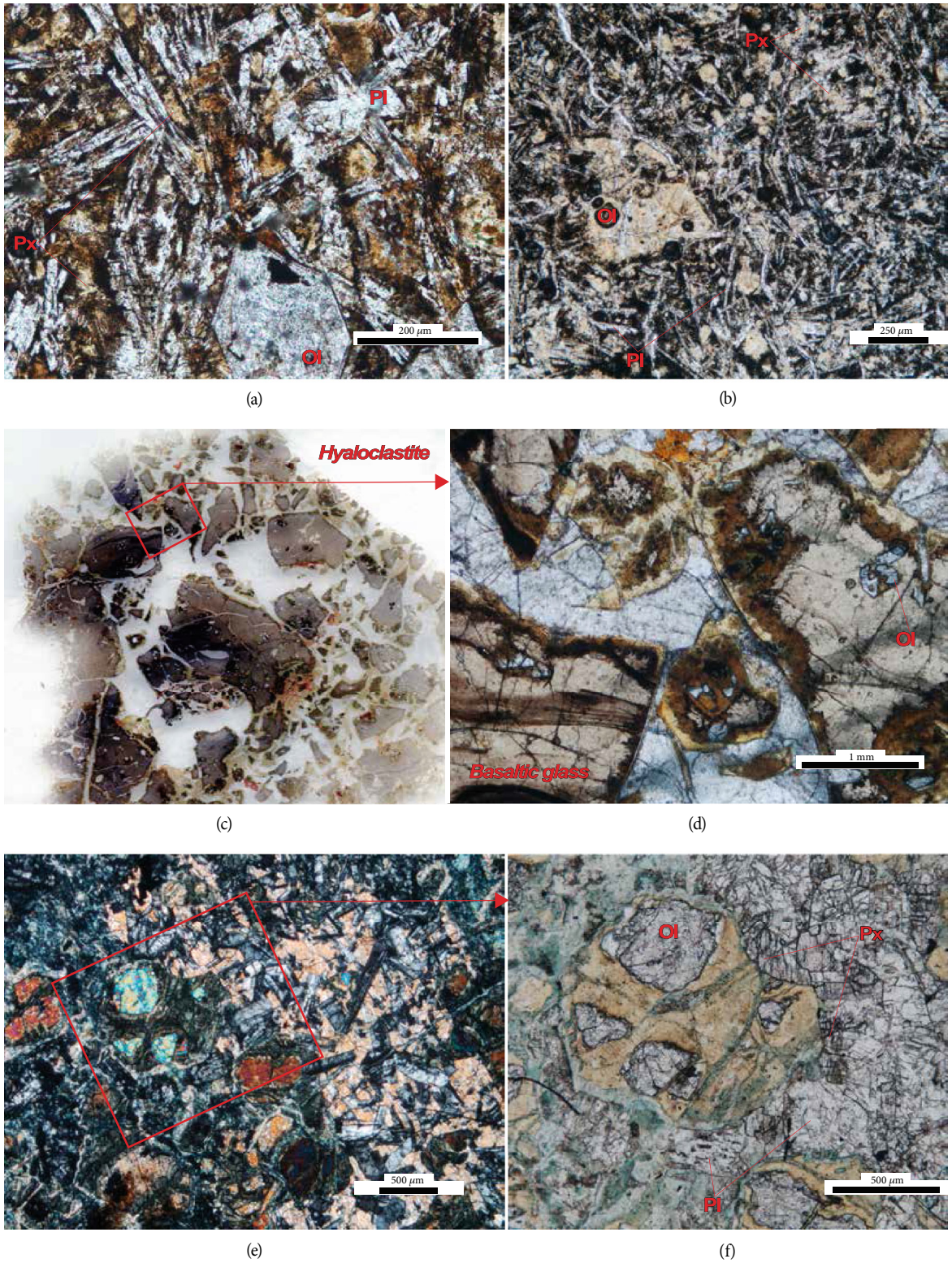

FIGURE 6: Microphotographs showing the main petrographic characteristics of the studied subaqueous and subvolcanic basaltic rocks in the Subbetic Basin. (a) Plane-polarized light (PPL) image of the inner microcrystalline area of a spherical pillow (Figure 4(a)). (b) PPL image of a highly altered basalt in a subaqueous deposit constituted by accumulated pillows (Figure 4(d)). (c) Thin section of a hyaloclastite interlayered with basaltic lava flows in the Alamedilla area. Irregular fragments and shards of glass are amalgamated by a calcareous cement. (d) PPL image of hyaloclastite basaltic glass fragments with Ol phenocrysts. (e) Cross-polarized light image of gabbroic textures that are characteristic of some subvolcanic sills and dikes in the Piletas area. (f) PPL detailed image of a serpentinized Ol phenocryst enclosed and partially reabsorbed in a subophitic Pl+Px matrix.

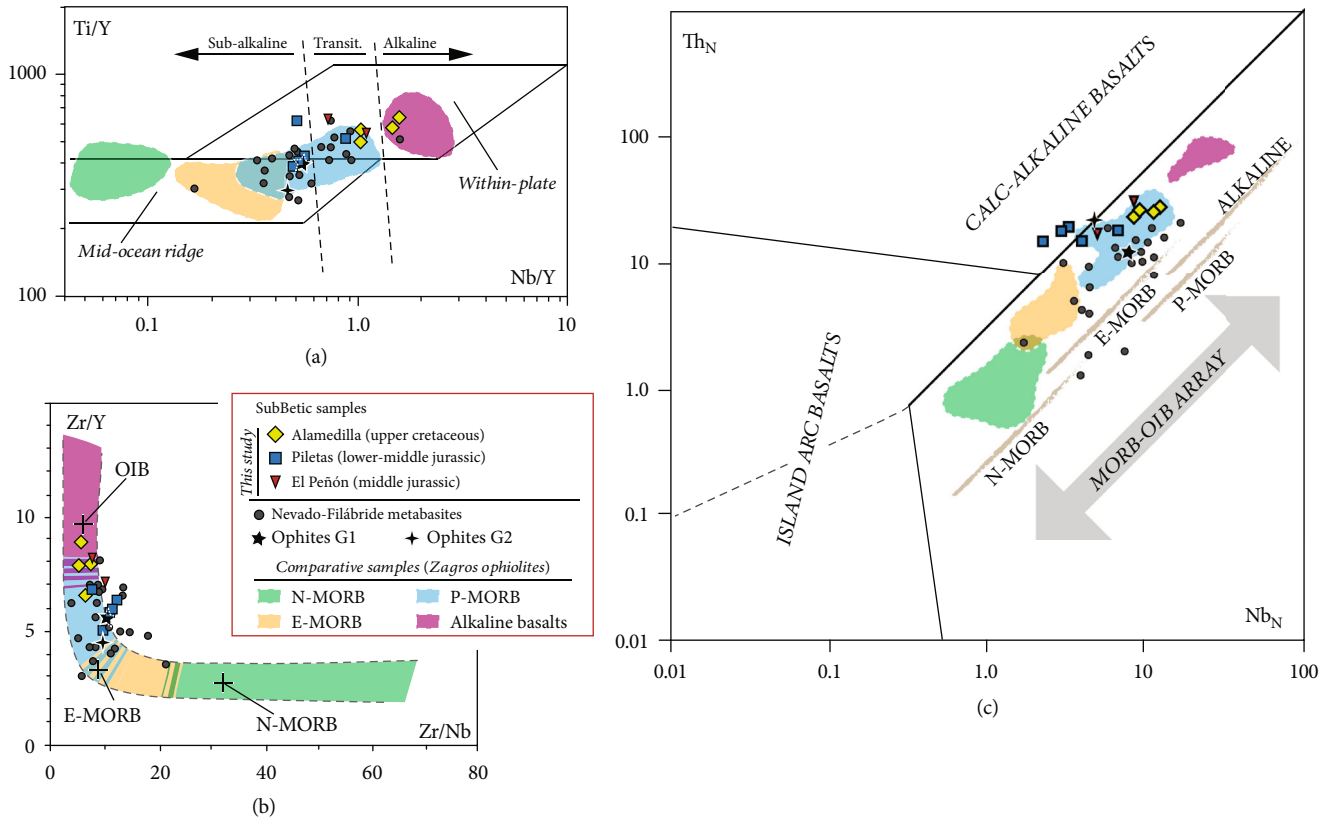

FIGURE 7: Geochemical characterization of the Subbetic basaltic magmatism. The samples collected in Alamedilla, Piletas, Cerro de los Peones, and El Peñón areas (Table 1) are plotted together with the Nevado-Filábride metabasalts [80] and the Triassic (Group 2) and Jurassic (Group 1) ophites [77]. Zagros ophiolites are included for comparison [82, 83]. Consider P-MORB comparatives as a compositional group (with enriched compositions), not related to a tectonic scenario. (a) Ti/Y vs. Nb/Y diagram (after [90]). (b) Zr/Y vs. Zr/Nb variation diagram showing the standardized compositions of MORB-, E-MORB-, and OIB-type basalts [91]. (c) N-MORB normalized Th vs. Nb discrimination diagram [93]. MORB-OIB array and subduction-related fields are defined according to the projection of a huge number of ophiolitic basalts.

(primarily HREE), and Zr, Nb, Ta, Y, Hf, and Th—have been demonstrated to be relatively immobile during low-temperature secondary processes (e.g., [86–89]). We tested the behavior of relevant (for this study) trace elements by means of variation diagrams vs. Zr (Supplementary material 1). Except for the most incompatible and mobile elements in basaltic melts, i.e., Rb, Ba, and Sr, trace elements show acceptable correlations with Zr, especially LREE. Therefore, alteration processes appear not to have involved significant variations in the content of the trace elements used to characterize the Subbetic basaltic magmatism. The departure of some Piletas basalts from the main trends (e.g., Th, Nb, and Ta) will be discussed below and compared with other geochemical characteristics in the context of their origin.

Regarding trace element compositions, the Alamedilla samples (Upper Cretaceous) show higher contents than the Piletas ones, except for the more compatible elements (Cr, Co, and V; Table 1; Supplementary material 1). Furthermore, the Alamedilla basalts present high Nb/Y values (1.1-1.6) and are plotted between the transitional and alkaline fields in the Ti/Y vs. Nb/Y diagram (Figure 7(a)) [90]. Cretaceous pillow lavas show Zr/Y ratios between 6 and 10, close to the composition of modern ocean-island basalts (OIB) (Figure 7(b)) [91]. Lower Nb/Y (<0.8) and Zr/Y ratios characterize the Piletas samples (Lower-Middle Jurassic), which are plotted together with the Jurassic and Triassic ophites (Groups 1 and 2, respectively) and the more scattered Nevado-Filábride ultramafic rocks (Figures 7(a) and 7(b)). Thus, the basaltic rocks of the Subbetic Basin present intermediate geochemical characteristics between alkaline or oceanic island basalts (OIB) and enriched mid-ocean ridge basalts (E-MORB) (e.g., [27, 82, 91, 92]): TiO_2 = 0.82 – 2.78, P_2O_5 = 0.11 – 0.40, Zr = 50.3 – 157.9, Y = 10.01 – 19.21, $(La/Yb)n$ = 2.6 – 6.8, Th/Yb = 1.28 – 2.29, and Ta/Yb = 0.05 – 1.59. Nevertheless, the Alamedilla samples consistently show higher trace element contents and a more alkaline signature than the Piletas ones (Figure 7).

According to the MORB-normalized Th vs. Nb diagram (Figure 7(c)), most of the studied samples are plotted along the MORB-OIB array. This projection is useful as a variation and tectonic discrimination diagram [93]. The similar behavior of Th and Nb during melting and fractionation processes maintains a reliable limit between subduction-related basalts and the MORB-OIB array, even for basaltic rocks that resulted from different melting/fractionation

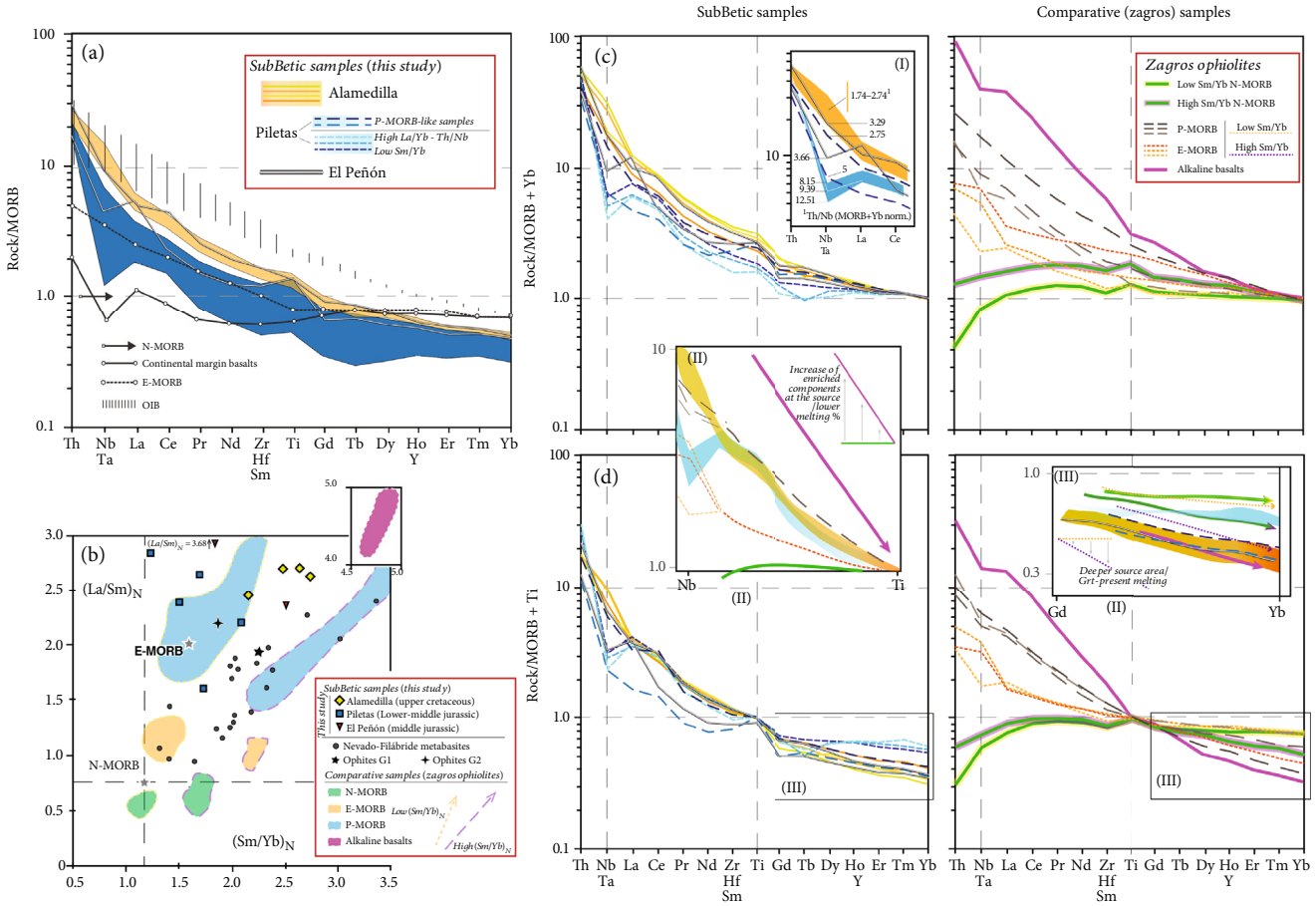

FIGURE 8: (a) N-MORB normalized trace elements patterns of the studied samples. Standard compositions of MORB, E-MORB, and OIB [91], and continental margin basalts [115] are plotted for comparison. (b) La/Sm vs. Sm/Yb variation diagram employed to summarize the relations between light, medium, and heavy REE (presented in Supplementary material 2). Stars represent N- and E-MORB averaged compositions from Gale et al. [116]. Comparative Zagros ophiolites describe two differentiated trajectories with low and high MREE/HREE ratios. Note that most of the studied samples show a positive correlation between La/Sm and Sm/Yb, except for the Piletas-type samples having the highest Th/Nb ratios. (c, d) Additional Yb and Ti normalization of the studied samples and the comparative data, following the methodology of Pearce [94]. According to the geochemical differences observed in the Piletas-type samples, they are split into two groups with differentiated La/Sm, Th/Nb, and Sm/Yb ratios. Inset (i) highlights the MORB+Yb normalized Nb-Ta negative anomalies observed in some of the Lower Jurassic samples. Insets (II) and (III) emphasize the MORB+Ti normalized patterns of the studied samples compared with Zagros ophiolites.

percentages. However, the nature of subduction-unrelated sources may be mixed up due to differential partial melting/-fractionation percentages. The studied Subbetic basalts present trace element compositions similar to the comparative P-MORB, with higher Th and Nb contents in the Upper Cretaceous samples, i.e., indicative of a more alkaline signature. Still, a significant group of the Jurassic basalts, together with the Triassic subvolcanic comparatives (Group 2 of the ophites), departs from the general trend of subduction-unrelated oceanic basalts towards calc-alkaline compositions (Figure 7(c)). This crustal geochemical input may be derived from the source or acquired during the ascent and emplacement of the basaltic melts.

The two samples collected in the El Peñón area within the Middle Jurassic Camarena Fm. present intermediate geochemical characteristics between the Early Jurassic and Late Cretaceous magmatism (Figure 7). ALM-9 sample represents a thick deposit of accumulated pillows. This basaltic rock shows high Th and Nb contents, together with high Nb/Y and Zr/Y ratios and is therefore close in composition to the more alkaline Alamedilla samples. In turn, the basaltic lava flow ALM-8 is quite similar to the Piletas samples and the Triassic ophites (Group 2) (Figure 7).

MORB-normalized trace element patterns of the studied samples highlight some characteristics of the Subbetic basaltic magmatism (Figure 8(a)): (i) pillow lavas and subvolcanic bodies are enriched in more incompatible elements (Th and LREE); (ii) these rocks show intermediate compositions between standardized enriched midocean ridge basalts and oceanic island basalts; (iii) the Alamedilla-type basalts (Upper Cretaceous) show higher trace element contents without major anomalies; and (iv) some of the Piletas samples (Lower to Middle Jurassic) present a deep Nb-Ta negative anomaly.

Regarding REE compositions, the Alamedilla samples and ALM-9 (El Peñón) present the highest ratios between

light, medium, and heavy REE (Figure 8(b), Supplementary material 2). The Piletas samples, ophites, and most of the Nevado-Filábride metabasalts show less steeped REE patterns. Zagros comparative data define two different trends with less fractionated HREE, i.e., positive slopes between normalized La/Sm and Sm/Yb ratios, and more fractionated samples with higher Sm/Yb ratios. The exception to this general REE behavior is a group of Piletas samples with increasing La/Sm values at decreasing Sm/Yb ratios (Figure 8(b)). These basaltic rocks depart from the MORB-OIB array in the Th vs. Nb diagram (Figure 7(c)).

We added Yb and Ti normalizations to the trace element contents referred to MORB, following the methodology of Pearce [94] (Figures 8(c) and 8(d)). The Yb normalization subtracts the effects of fractional crystallization from the original melt/rock fractionation of more incompatible trace elements. The Subbetic Cretaceous basaltic rocks are enriched in incompatible elements and LREE with respect to Jurassic magmatism. The latter includes samples with different trace element patterns: three samples present particularly high Th/Nb and La/Sm ratios, together with low Sm/Yb values (Figure 8(c)); the remaining Jurassic samples show flatter trace element patterns and similar compositions to other enriched or plume-related MORB. An additional Ti normalization emphasizes the behavior of the least incompatible elements (HREE), which depends on the stability of Grt at the solid assemblage and, hence, on the source depth. The patterns of more incompatible trace elements may be interpreted according to the nature of the mantle source and/or the melting percentage (Figure 8(d)). In this regard, the Alamedilla and Piletas samples have similar slopes, close in composition to the Zagros P-MORB. A significant exception is constituted by the Piletas samples with deep Nb-Ta negative anomalies. When compared with the Zagros ophiolites, the Alamedilla samples show steep HREE patterns similar to the enriched magmatism with high Sm/Yb ratios. Flatter HREE patterns among the Subbetic samples were observed in the Piletas basalts, with negative Nb-Ta anomalies.

6. Discussion

6.1. Variation of Basaltic Melts and Mantle Sources during Rifting Evolution. The basaltic rocks of the Subbetic Basin reveal a volumetrically poor magmatic response to Mesozoic rifting in the South Iberian continental margin. These magmas are interspersed in Triassic, Jurassic, and Cretaceous sediments, either as subaqueous lava flows or shallow subvolcanic sills and dikes (the so-called ophites), the latter being more frequent in older formations (Figures 1–3).

The geochemical study of the Mesozoic basalts in the Subbetic Basin shows a mostly homogeneous magmatism along the protracted rifting process, characterized by enriched compositions in incompatible elements and LREE with respect to MORB. Nevertheless, the higher Ti, Zr, Th, and Nb contents observed in the Cretaceous samples evidence an increase in the alkaline signature of the younger magmas. Similar geochemical evolutions have been described in coeval rift-related magmatism of the North Iberian plate margins (e.g., [95]).

The Piletas-type samples (except ALM-13) show high #Mg values (0.64-0.73), which suggest that immobile element variations are derived from the source, discarding significant in situ fractionation processes. Petrographic observations (Figure 6), together with the short-range trace element variations vs. Zr (Supplementary material 1) and the presence of positive and negative Eu anomalies (Supplementary material 2), point to a likely Ol+Pl±Px fractionation during ascent and emplacement of the basaltic melts. This process may have been favored by the building of an incipient magmatic plumbing system at upper crustal levels, as suggested by the presence of gabbroic rocks and the dominant sills and dikes observed in the Triassic and Jurassic formations. Lower #Mg and Al_2O_3/TiO_2 values characterize the Alamedilla-type pillow lavas. Such features, together with the slightly negative Eu anomalies, would indicate a similar Ol+Pl±Px in situ fractionation for the younger magmatism (Supplementary material 1 and 2). Nevertheless—according to the enriched Th, Nb, Ti, and LREE compositions, the steep trace element patterns after MORB, Yb, and Ti normalizations, and the differentiated behavior of LREE/HREE ratios vs. Zr (inferred fractionation trends) (Figure 8, Supplementary material 1)—trace element contents and ratios also account for the nature of mantle sources and melting conditions and highlight important differences between the Cretaceous and the Triassic/Jurassic Subbetic magmatism. Similarly, incompatible and LREE in the Subbetic basalts show positive correlations vs. Zr (a proxy of the melting/-fractionation progress) and present similarly steep patterns that relate this magmatism to enriched mantle sources. In contrast, HREE (e.g., Y and Yb; Supplementary material 1) show constant values in the Cretaceous Alamedilla-type samples. The fact that these basalts show steep positive correlations between Ce/Y, Th/Yb, or Ce/Yb and Zr would suggest the stability of a mineral phase that captured HREE at the source (e.g., Grt) (Figure 8, Supplementary material 1).

The Th/Yb vs. Nb/Yb and TiO_2/Yb vs. Nb/Yb projections (Figures 9(a) and 9(b)) [94] summarize the results of the previously described Th vs. Nb diagram and MORB, Yb, and Ti normalized trace element patterns (Figures 7(c) and 8). The Piletas samples, especially those with higher Nb-Ta negative anomalies (Figure 8), depart from the MORB-OIB array. The vertical trends depicted by these older basalts, and the Upper Triassic subvolcanic (Group 2; [77]) and volcanic rocks (Zamoranos Fm.; [79]), entail a subduction-related geochemical signature that may reflect the presence of crustal components, within the source or acquired during the ascent and emplacement of the basaltic melts. This crustal signature can be modeled in terms of Amp-bearing lherzolites (Figures 9(c)–9(e)). The departure of the Piletas samples with steep Nb-Ta anomalies from the typical melting/fractionation trend depicted by Spl- or Grt-bearing lherzolites (Ce/Y vs. Zr/Nb; Figure 9(c)), together with the negative correlation between Zr/Sm vs. Ce/Y and La/Yb vs. Dy/Yb ratios (Figures 9(d) and 9(e)), can be explained by the buffering effect of Amp over the MREE in mantle sources [96]. Regarding regional

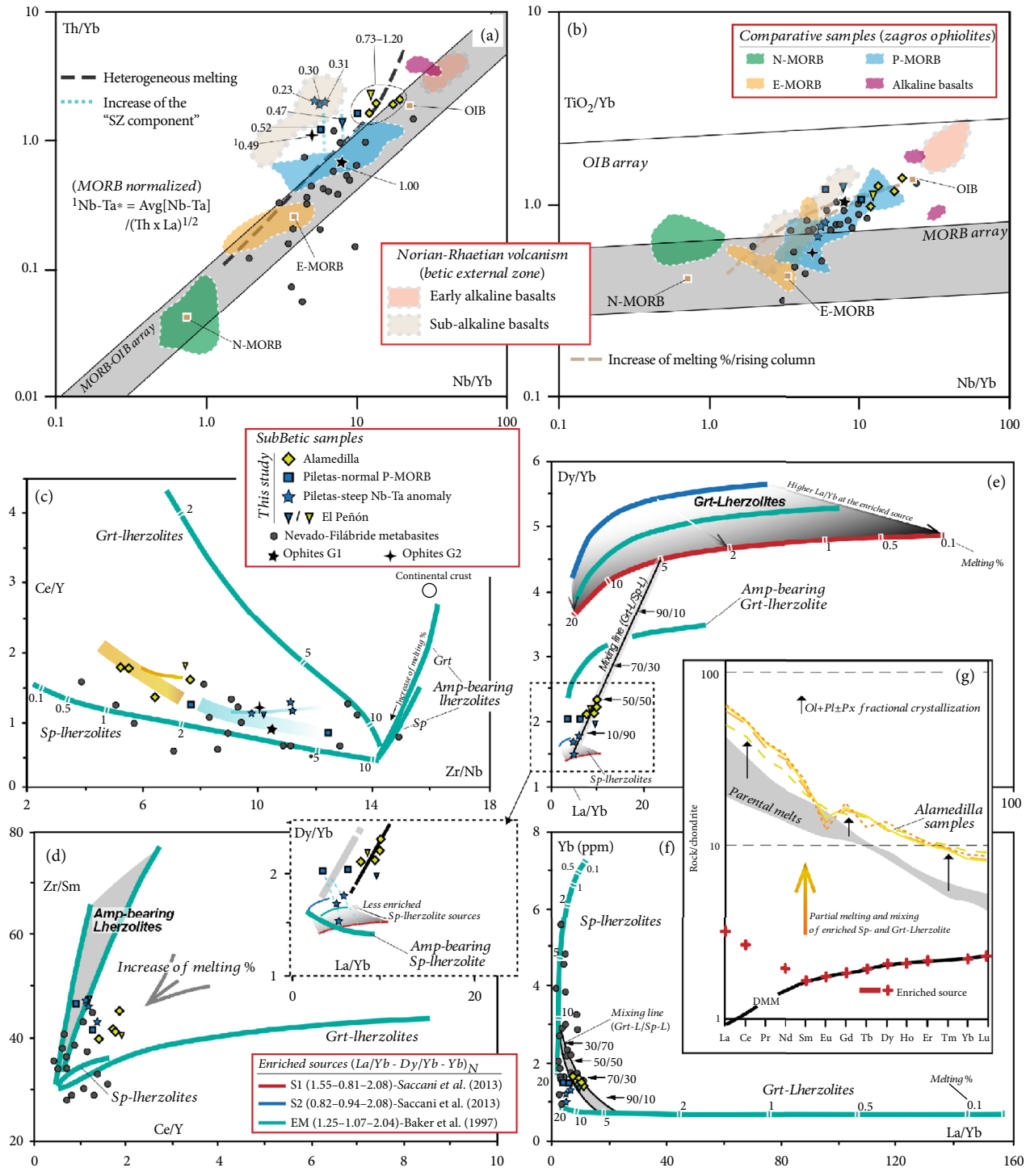

FIGURE 9: (a, b) Th/Yb vs. Nb/Yb and TiO_2/Yb vs. Nb/Yb [94]. These plots serve as tectonic discrimination diagrams and yield relevant petrogenetic information about the nature and the conditions at the source. See discussion for further details. Note that Middle Jurassic samples (El Peñón) are colored according to their geochemical affinity with Alamedilla- (yellow) or Piletas-type (blue) basalts. (c, d) Variation diagrams of Ce/Y vs. Zr/Nb and Zr/Sm. Modeled fractional melts of Amp-, Grt-, and Sp-lherzolites and averaged continental crust composition modified from Baker et al. [96]. (e, f) Variation diagrams of La/Yb vs. Dy/Yb and Yb indicating possible source compositions, melting percentages, and mixing proportions between melts derived from Spl- and Grt-bearing mantle sources for the Subbetic basalts. The modeled melt curves represent different sources enriched in LREE [82, 96]. In addition, the inset of Figure 8(e) shows the location of the melting curve of Amp+Spl-lherzolites. (g) Modeled fractional crystallization of Ol+Pl±Px. A 60/40 proportion was selected for the mineral assemblage; 20-30% of fractional crystallization results in the REE composition of Alamedilla samples. The S1-enriched source and the parental melts obtained after different melting percentages and mixing of Grt- and Spl-facies melts were obtained from Saccani et al. [83]. DMM: depleted mantle.

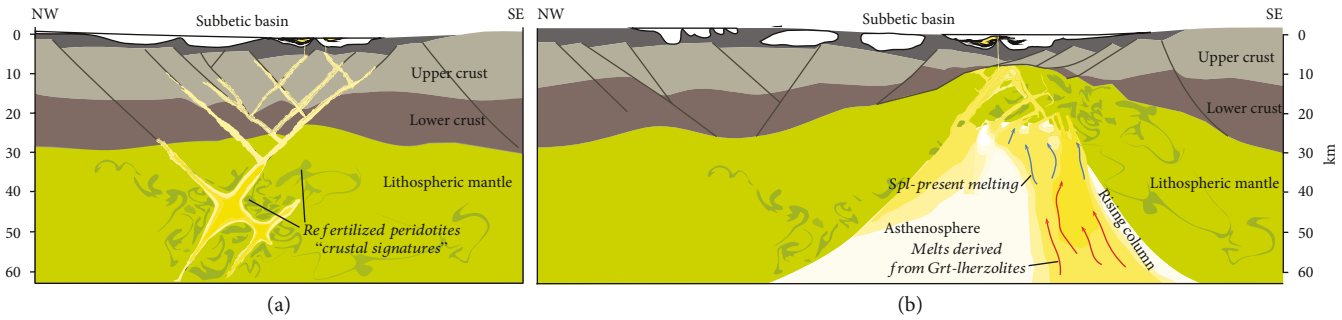

FIGURE 10: Schematic evolution of the magmatism in the Subbetic Basin during Early Jurassic syn-rift stage (a) and Early Cretaceous hyperextension (b).

comparative data, the younger subvolcanic rocks (Group 1 of the ophites) resemble an averaged composition of the scattered Nevado-Filábride metabasalts and may derive from the uncontaminated and enriched mantle source of Triassic-Jurassic magmatism (Figures 9(a) and 9(b)). These geochemical characteristics and the restored cross-section (Figure 3) relate the Subbetic and the Nevado-Filábride samples and preclude that these metabasalts might come from the metamorphism of remnants of a mature (N-MORB-type) oceanic crust.

The Alamedilla samples are close in composition to typical OIB basalts (Figures 8, 9(a), and 9(b)). According to numerical models, these enriched compositions slightly above the MORB-OIB array could derive from the heterogeneous melting of a contaminated and enriched source, when the process entailed very low melting percentages [94]. Accordingly, the less refractory source material with high Th/Nb ratios might be involved. However, some evidence points to a deeper source for the Cretaceous Subbetic basalts: (i) the steep HREE patterns (Figure 8); (ii) the positive correlation between melting/fractionation progress (increase of Zr content or decrease of #Mg) and LREE/HREE ratios (Supplementary material 1). The trends defined by the Alamedilla-type basalts between the modeled compositions of enriched Spl- and Grt-lherzolites suggest the presence of melts from deep and shallower sources (Figures 9(c)–9(f)). The mixing proportions and melting percentages depend on the enrichment factor of the mantle sources (light, medium, and heavy REE ratios) [82, 96]. According to the Dy/Yb and La/Yb ratios (Figure 9(e)), in the case of highly enriched sources, a 50/50 to 70/30 mix between low melting percentages (<10%) of Spl- and Grt-lherzolites, respectively, might have generated the Cretaceous Subbetic magmatism. The subsequent 20-30% fractionation of a solid assemblage constituted by Ol+Pl±Px could reproduce the incompatible and rare earth element patterns observed in the Alamedilla-type samples (Figure 9(g)). These variation diagrams suggest that the Triassic/Jurassic magmatism that was not significantly modified by contaminated sources or assimilation processes (ophites G1 and Piletas samples without significant Nb-Ta anomaly) also entails the presence of melts derived from Grt-lherzolites or from the Grt+Sp-lherzolite stability field. Tentatively, these older basalts resulted from higher melting percentages and lower melt proportion originated at deeper sources (Grt-present melting) in comparison with Cretaceous magmatism (Figure 9).

6.2. Melt-Weakening Processes. The timing and nature of the limited magmatism in magma-poor rifted basins provide important clues for discerning the deformation mode. A number of opposing kinematic models attempt to explain crustal hyperextension. One group proposes distributed normal faulting within the upper crust acting sequentially in time and coeval to ductile deformation of the lower crust [24, 97–99]. Alternatively, hyperextension can result from slip on a lithospheric-scale fault that finally acts as a large-scale detachment exhuming serpentinized mantle (e.g., [15, 23, 100, 101]).

Our results reveal that the onset of mantle partial melting began during an early stage of continental rifting, recorded by facies and thickness variations at the basin scale. Interlayered basalts within the Zegrí Fm. (Piletas-type samples) apparently recorded this process, suggesting that melting and deformation occurred within the lithospheric mantle at the onset of the rifting. Accordingly, our data indicate that the lithospheric-scale deformation governed the evolution of the continental rifting at the South Iberian paleomargin from the earliest stages, melt-weakening processes acting on a rifting event with limited magma production. This conclusion may back up the results obtained in other hyperextended basins (e.g., [29, 33]).

The Subbetic Basin developed on the Southern Iberian pre-Mesozoic crust, a region that previously underwent Variscan orogenesis at a late Paleozoic time. Major WNW-ESE trending lithospheric shear zones and faults constitute the boundaries of the main Variscan continental domains (e.g., [34]). The Jurassic-Early Cretaceous transfer faults that segmented the South Iberian paleomargin run parallel to these Variscan boundaries, probably playing an important role in triggering segmentation and oblique rifting. Moreover, the aeromagnetic map of Southern Iberia [102] reveals that the WNW-ESE trend of the Variscan structures runs parallel to the elongated magnetic dipoles that extend beneath the Guadalquivir foreland basin and the Jurassic-Early Cretaceous transfer faults (Figure 1(a)) [44].

The positive feedback between mantle melting, weakening processes, and lithospheric-scale detachments calls for the presence of fertile peridotites in the upper mantle.

Hence, we interpret that the crustal signature of the Jurassic basalts and the Upper Triassic ophites and volcanic rocks (deep Nb-Ta negative anomalies and high Th/Nb ratios) was acquired at the mantle source. Bits of evidence serve to discard the contamination of older basaltic melts during ascent and emplacement processes in the crust: (i) the rapid quenching of sills and dikes prevented the geochemical interaction between the intruding melts and the host upper crustal rocks and (ii) an increasingly thin crust and the volumetrically poor magmatism did not favor the building of a thermal dome in the lower crust where basaltic melts could have assimilated crustal rocks and/or enhanced crustal anatexis [103, 104]. Furthermore, a few tens of km north of the study area, Cenozoic volcanic rocks contain xenoliths of refertilized Amp-lherzolites, probably associated with a Paleozoic suprasubduction mantle [105, 106].

In the absence of an active subduction or mantle plume in the Mesozoic rifted margin of Southern Iberia, the presence of fertile ultramafic lithologies along with the attenuated crustal thickness most likely exerted major control upon the basaltic magmatism [28, 30]. Any anticipated direct relation between crustal thickness and Grt-signature in the melting products is lacking in the hyperextended Subbetic margin. Contrariwise, the initial rifting stages were dominated by partial melting of shallower areas of the mantle dominated by refertilized lherzolites (Figure 10(a)). These mantle regions modified by ancient crustal components—having melted at higher pressures than host peridotites at the same potential mantle temperature—would have enhanced lithospheric weakening [28, 107]. Subsequently, the Grt signal increased and the crustal signature decreased in the Subbetic basalts during rifting evolution. These characteristics suggest the development of a rising mantle column and a proportional increase of the liquids derived from Grt-present melting (Figure 10(b)).

Considering the conspicuous traces of Paleozoic subductive remnants in the margins of Iberia, the presence of Grt-pyroxenites, originated by the reaction of high-silica melts (derived from eclogites) and peridotites, is a feasible hypothesis [28]. We assume that the high MREE/HREE ratios in the Subbetic basalts are due to partial melting of deep lherzolites in the Grt stability field (modeled above; Figure 9). Still, the putative presence of pyroxenites as Grt-signature donors which are stable at shallower mantle regions cannot be dismissed and should be evaluated in the future (e.g., [108–113]).

7. Conclusion

The composition of submarine volcanic rocks from the Subbetic hyperextended basin yields new insight into the mechanical behavior of the subcontinental mantle during continental rifting. Basaltic volcanism—along the rift axis during crustal attenuation—interacted with sedimentary packages sinking into underlying evaporate/clay-rich rocks. The geochemical characteristics of volcanic rocks evolved during the extensional process: (i) Cretaceous basaltic magmatism, coeval with crustal hyperextension and postrift stages, records highly enriched MORB compositions; the moderate Sm/Yb values and the positive correlation between LREE/HREE and Zr point to the involvement of deep (Grt-present) mantle sources in the origin of late basaltic melts; (ii) conversely, the Lower to Middle Jurassic syn-rift basalts feature less enriched MORB compositions, moderate La/Sm, and low Sm/Yb ratios, with deep Nb-Ta negative anomalies and high Th/Nb ratios in most of the samples.

Mantle-derived basalts interlayered within the Lower Jurassic syn-rift deposits suggest that melting and deformation within the lithospheric mantle began early during continental rifting. We interpret this initially enriched stage as a signal of partial melting of recycled crustal rocks within the upper mantle, associated with remnants of pre-Mesozoic subducted slabs. The melt-weakening process could therefore explain the inception of lithospheric-scale shear zones controlling the evolution of magma-poor hyperextension, which progressed until Cretaceous times, with the activation of deeper melt sources in the mantle and an increase of the alkaline signature in the basaltic deposits.

Data Availability

All data supporting the results of our study can be found in the figures, tables, and supplementary material submitted to the journal.

Conflicts of Interest

The authors declare that they have no conflicts of interest.

Acknowledgments

This work was supported by grants from the Spanish Geological Survey (Tectonic Map of the Iberian Peninsula and the Surrounding Cordilleras), the Junta de Andalucía (A-RNM-005-UGR18 and FIPS, PY20-01387), and the Spanish Science Ministry (REViSE-Betics-PID2020-119651RB-I00). Jean Sanders corrected the English writing style.

Supplementary Materials

Supplementary material 1: trace element contents and ratios vs. Zr. Supplementary material 2: chondrite-normalized REE diagrams. *(Supplementary Materials)*

References

[1] R. W. Bialas, W. R. Buck, and R. Qin, "How much magma is required to rift a continent?," *Earth and Planetary Science Letters*, vol. 292, no. 1-2, pp. 68–78, 2010.

[2] W. R. Buck, "Consequences of asthenospheric variability on continental rifting," in *Rheology and Deformation of the Lithosphere at Continental Margins*, G. D. Karner, Ed., pp. 1–30, Columbia Univ. Press, New York, 2004.

[3] J.-M. Kendall, G. W. Stuart, C. J. Ebinger, I. D. Bastow, and D. Keir, "Magma-assisted rifting in Ethiopia," *Nature*, vol. 433, no. 7022, pp. 146–148, 2005.

[4] A. Festa, G. Balestro, A. Borghi, S. de Caroli, and A. Succo, "The role of structural inheritance in continental break-up and exhumation of Alpine Tethyan mantle (Canavese zone,

Western Alps)," *Geoscience Frontiers*, vol. 11, no. 1, pp. 167–188, 2020.

[5] C. J. Ebinger and M. Casey, "Continental breakup in magmatic provinces: An Ethiopian example," *Geology*, vol. 29, no. 6, pp. 527–530, 2001.

[6] G. Corti, J. van Wijk, S. Cloetingh, and C. K. Morley, "Tectonic inheritance and continental rift architecture: numerical and analogue models of the East African Rift system," *Tectonics*, vol. 26, no. 6, article TC6006, 2007.

[7] C. K. Morley, *Influence of Preexisting Fabrics on Rift Structure*, Geoscience of Rift Systems—Evolution of East Africa, 1999.

[8] C. K. Morley, "Stress re-orientation along zones of weak fabrics in rifts: An explanation for pure extension in 'oblique' rift segments?," *Earth and Planetary Science Letters*, vol. 297, no. 3-4, pp. 667–673, 2010.

[9] A. R. Samsu, A. R. Cruden, N. E. Molnar, and R. F. Weinberg, "Inheritance of penetrative basement anisotropies by extension-oblique faults: insights from analogue experiments," *Tectonics*, vol. 40, no. 5, article e2020TC006596, 2021.

[10] W. R. Buck, "Modes of continental lithospheric extension," *Journal of Geophysical Research*, vol. 96, no. B12, pp. 20161–20178, 1991.

[11] E. B. Burov, "Rheology and strength of the lithosphere," *Marine and Petroleum Geology*, vol. 28, no. 8, pp. 1402–1443, 2011.

[12] S. Cloetingh, E. Burov, L. Matenco, F. Beekman, F. Roure, and P. A. Ziegler, "The Moho in extensional tectonic settings: insights from thermo-mechanical models," *Tectonophysics*, vol. 609, pp. 558–604, 2013.

[13] R. Huismans and C. Beaumont, "Depth-dependent extension, two-stage breakup and cratonic underplating at rifted margins," *Nature*, vol. 473, no. 7345, pp. 74–78, 2011.

[14] R. S. Huismans and C. Beaumont, "Complex rifted continental margins explained by dynamical models of depth-dependent lithospheric extension," *Geology*, vol. 36, no. 2, pp. 163–166, 2008.

[15] R. S. Huismans and C. Beaumont, "Roles of lithospheric strain softening and heterogeneity in determining the geometry of rifts and continental margins," *Geological Society, London, Special Publications*, vol. 282, no. 1, pp. 111–138, 2007.

[16] P. A. Ziegler and S. Cloetingh, "Dynamic processes controlling evolution of rifted basins," *Earth Science Reviews*, vol. 64, no. 1-2, pp. 1–50, 2004.

[17] L. Geoffroy, "Les marges passives volcaniques," *Comptes Rendus Geoscience*, vol. 337, no. 16, pp. 1395–1408, 2005.

[18] L. Geoffroy, E. B. Burov, and P. Werner, "Volcanic passive margins: another way to break up continents," *Science Reports*, vol. 5, no. 1, p. 14828, 2015.

[19] E. Rampone, G. Borghini, and V. Basch, "Melt migration and melt-rock reaction in the Alpine-Apennine peridotites: insights on mantle dynamics in extending lithosphere," *Geoscience Frontiers*, vol. 11, no. 1, pp. 151–166, 2020.

[20] G. Corti, M. Bonini, F. Innocenti, P. Manetti, G. B. Piccardo, and G. Ranalli, "Experimental models of extension of continental lithosphere weakened by percolation of asthenospheric melts," *Journal of Geodynamics*, vol. 43, no. 4-5, pp. 465–483, 2007.

[21] G. Ranalli, G. B. Piccardo, and P. Corona-Chávez, "Softening of the subcontinental lithospheric mantle by asthenosphere melts and the continental extension/oceanic spreading transition," *Journal of Geodynamics*, vol. 43, no. 4-5, pp. 450–464, 2007.

[22] H. Wallner and H. Schmeling, "Experimental models of extension of continental lithosphere weakened by percolation of asthenospheric melts," *Journal of Geodynamics*, vol. 43, no. 4-5, pp. 465–483, 2007.

[23] G. Manatschal, "New models for evolution of magma-poor rifted margins based on a review of data and concepts from West Iberia and the Alps," *International Journal of Earth Sciences*, vol. 93, no. 3, pp. 432–466, 2004.

[24] T. J. Reston and K. G. McDermott, "Successive detachment faults and mantle unroofing at magma-poor rifted margins," *Geology*, vol. 39, no. 11, pp. 1071–1074, 2011.

[25] Y. Dilek, H. Furnes, and M. Shallo, "Geochemistry of the Jurassic Mirdita Ophiolite (Albania) and the MORB to SSZ evolution of a marginal basin oceanic crust," *Lithos*, vol. 100, no. 1-4, pp. 174–209, 2008.

[26] Y. Dilek and H. Furnes, "Ophiolites and their origins," *Elements*, vol. 10, no. 2, pp. 93–100, 2014.

[27] E. Saccani, Y. Dilek, M. Marroni, and L. Pandolfi, "Continental margin ophiolites of Neotethys: remnants of ancient ocean-continent transition zone (OCTZ) lithosphere and their geochemistry, mantle sources and melt evolution patterns," *Episodes*, vol. 38, no. 4, pp. 230–249, 2015.

[28] A. V. Sobolev, A. W. Hofmann, D. V. Kuzmin et al., "The amount of recycled crust in sources of mantle derived melts," *Science*, vol. 316, no. 5823, pp. 412–417, 2007.

[29] M. Amann, M. Ulrich, G. Manatschal et al., "Geochemical characteristics of basalts related to incipient oceanization: the example from the Alpine-Tethys OCTs," *Terra Nova*, vol. 32, no. 1, pp. 75–88, 2020.

[30] Y. Niu, "Lithosphere thickness controls the extent of mantle melting, depth of melt extraction and basalt compositions in all tectonic settings on Earth - a review and new perspectives," *Earth Science Reviews*, vol. 217, p. 103614, 2021.

[31] Y. Dilek, E. M. Moores, and H. Furnes, "Structure of modern oceanic crust and ophiolites and implications for faulting and magmatism at oceanic spreading centers," *American Geophysical Union Monograph*, vol. 106, pp. 219–265, 1998.

[32] Y. Dilek and H. Furnes, "Ophiolite genesis and global tectonics: geochemical and tectonic fingerprinting of ancient oceanic lithosphere," *Geological Society of America Bulletin*, vol. 123, no. 3-4, pp. 387–411, 2011.

[33] M.-A. Kaczmarek and O. Müntener, "Juxtaposition of melt impregnation and High-Temperature shear zones in the upper mantle; field and petrological constraints from the Lanzo peridotite (northern Italy)," *Journal of Petrology*, vol. 49, no. 12, pp. 2187–2220, 2008.

[34] A. Azor, I. Dias da Silva, J. Gómez Barreiro et al., "Deformation and structure," in *The Geology of Iberia: A Geodynamic Approach, Regional Geology Reviews*, C. Quesada and J. T. Oliveira, Eds., pp. 307–348, Springer, 2019.

[35] D. Martínez Poyatos, R. Carbonell, I. Palomeras et al., "Imaging the crustal structure of the central Iberian zone (Variscan Belt): the ALCUDIA deep seismic reflection transect," *Tectonics*, vol. 31, no. 3, article TC3017, 2012.

[36] J. F. Simancas, R. Carbonell, F. González Lodeiro et al., "crustal structure of the transpressional Variscan Orogen of SW Iberia: SW Iberia deep seismic reflection profile (IBERSEIS)," *Tectonics*, vol. 22, no. 6, p. 1062, 2003.

[37] J. F. Simancas, P. Ayarza, A. Azor et al., "A seismic geotraverse across the Iberian Variscides: orogenic shortening, collisional magmatism and orocline development," *Tectonics*, vol. 32, no. 3, pp. 417–432, 2013.

[38] C. Quesada, O. Apalategui, L. Eguiluz, E. Liñán, and T. Palacios, "Part V: Ossa-Morena zone," in *Pre-Mesozoic Geology of Iberia*, R. D. Dallmeyer and E. Martínez García, Eds., pp. 252–258, Springer, Berlin, 1990.

[39] R. Sánchez Carretero, L. Eguíluz, E. Pascual, and M. Carracedo, "Ossa-Morena zone: igneous rocks," in *Pre-Mesozoic Geology of Iberia*, R. D. Dallmeyer and E. Martínez García, Eds., pp. 292–313, Springer Verlag, Berlin, 1990.

[40] J. F. Simancas, I. Expósito, A. Azor, D. Martínez Poyatos, and F. González Lodeiro, "From the Cadomian orogenesis to the early Palaeozoic Variscan rifting in Southwest Iberia," *Journal of Iberian Geology*, vol. 30, pp. 53–71, 2004.

[41] J. Vergés and M. Fernàndez, "Tethys-atlantic interaction along the Iberia-Africa plate boundary: the betic-rif orogenic system," *Tectonophysics*, vol. 579, pp. 144–172, 2012.

[42] C. Faccenna, C. Piromallo, A. Crespo-Blanc, L. Jolivet, and F. Rossetti, "Lateral slab deformation and the origin of the western Mediterranean arcs," *Tectonics*, vol. 23, no. 1, article TC1012, 2004.

[43] L. Lonergan and N. White, "Origin of the Betic-Rif mountain belt," *Tectonics*, vol. 16, no. 3, pp. 504–522, 1997.

[44] A. Pedrera, A. Ruiz-Constán, J. García-Senz et al., "Evolution of the south-Iberian paleomargin: from hyperextension to continental subduction," *Journal of Structural Geology*, vol. 138, p. 104122, 2020.

[45] P. Fallot, "Betic Cordilleras," *Estudios Geológicos*, vol. 4, pp. 259–279, 1948.

[46] J. M. Azañón, J. Galindo-Zaldívar, V. García-Dueñas, and A. Jabaloy, "Alpine tectonics II: Betic cordillera and Balearic Islands," in *Geology of Spain, Geological Society, London Special Publication*, T. Moreno and J. Wesley, Eds., pp. 401–416, Geology of Spain, London (UK), 2003.

[47] A. Jabaloy-Sánchez, J. A. Padrón-Navarta, M. T. Gómez-Pugnaire, V. López Sánchez-Vizcaíno, and C. J. Garrido, "Alpine orogeny: deformation and structure in the southern Iberian margin (Betics s.l.)," in *The Geology of Iberia: A Geodynamic Approach. Regional Geology Reviews*, C. Quesada and J. Oliveira, Eds., Springer, 2019.

[48] W. M. Behr and J. P. Platt, "Kinematic and thermal evolution during two-stage exhumation of a Mediterranean subduction complex," *Tectonics*, vol. 31, no. 4, article TC4025, 2012.

[49] M. T. Gómez-Pugnaire, J. Galindo-Zaldívar, D. Rubatto, F. González-Lodeiro, V. López Sánchez-Vizcaíno, and A. Jabaloy, "A reinterpretation of the Nevado-Filábride and Alpujárride complexes (Betic Cordillera): field, petrography and U-Pb ages from orthogneisses (western Sierra Nevada, S Spain)," *Schweizerische Mineralogische und Petrographische Mitteilungen*, vol. 84, pp. 303–322, 2004.

[50] V. L. Sánchez-Vizcaíno, D. Rubatto, M. T. Gómez-Pugnaire, V. Trommsdorff, and O. Müntener, "Middle Miocene high-pressure metamorphism and fast exhumation of the Nevado-Filábride complex, SE Spain," *Terra Nova*, vol. 13, no. 5, pp. 327–332, 2001.

[51] J. P. Platt, R. Anczkiewicz, J. I. Soto, S. P. Kelley, and M. Thirlwall, "Early Miocene continental subduction and rapid exhumation in the western Mediterranean," *Geology*, vol. 34, no. 11, pp. 981–984, 2006.

[52] M. T. Gómez-Pugnaire, D. Rubatto, J. M. Fernández-Soler et al., "Late Variscan magmatism in the Nevado-Filabride Complex: U-Pb geochronologic evidence for the pre-Mesozoic nature of the deepest Betic complex (SE Spain)," *Lithos*, vol. 146-147, pp. 93–111, 2012.

[53] J. Galindo-Zaldivar, F. Gonzalez-Lodeiro, and A. Jabaloy, "Progressive extensional shear structures in a detachment contact in the Western Sierra Nevada (Betic Cordilleras, Spain)," *Geodinamica Acta*, vol. 3, no. 1, pp. 73–85, 1989.

[54] A. Jabaloy, J. Galindo-Zaldívar, and F. González-Lodeiro, "The Alpujarride-Nevado-Fibabride extensional shear zone, Betic Cordillera, SE Spain," *Journal of Structural Geology*, vol. 15, no. 3-5, pp. 555–569, 1993.

[55] J. C. Balanyá, A. Crespo-Blanc, M. Díaz Azpiroz, I. Expósito, and M. Luján, "Structural trend line pattern and strain partitioning around the Gibraltar Arc accretionary wedge: insights as to the mode of orogenic arc building," *Tectonics*, vol. 26, no. 2, article TC2005, 2007.

[56] A. Crespo-Blanc, "Superimposed folding and oblique structures in the palaeomargin-derived units of the Central Betics (SW Spain)," *Journal of the Geological Society of London*, vol. 164, no. 3, pp. 621–636, 2007.

[57] J. F. Flinch and J. I. Soto, "Allochthonous Triassic and salt tectonic processes in the Betic-Rif orogenic arc," in *Permo-Triassic salt provinces of Europe, North Africa and the Atlantic margins*, J. I. Soto, J. F. Flinch, and G. Tari, Eds., pp. 417–446, Elsevier Inc., 2017.

[58] A. Pedrera, C. Marín-Lechado, S. Martos-Rosillo, and F. J. Roldán, "Curved fold-and-thrust accretion during the extrusion of a synorogenic viscous allochthonous sheet: the Estepa range (external zones, Western Betic cordillera, Spain)," *Tectonics*, vol. 31, no. 4, article TC4013, 2012.

[59] A. Pedrera, C. Marín-Lechado, J. Galindo-Zaldívar, and J. L. García-Lobón, "Control of preexisting faults and near-surface diapirs on geometry and kinematics of fold-and-thrust belts (internal Prebetic, eastern Betic Cordillera)," *Journal of Geodynamics*, vol. 77, pp. 135–148, 2014.

[60] J. P. Platt, S. Allerton, A. Kirker et al., "The ultimate arc: differential displacement, oroclinal bending, and vertical axis rotation in the external Betic-Rif arc," *Tectonics*, vol. 22, no. 3, p. 1017, 2003.

[61] M. García-Hernández, A. C. López-Garrido, P. Rivas, C. Sanz de Galdeano, and J. A. Vera, "Mesozoic palaeogeographic evolution of the external zones of the Betic Cordillera," *Geologie en Mijnbouw*, vol. 59, no. 2, pp. 155–168, 1980.

[62] A. Martín-Algarra and J. A. Vera, "The Betic cordillera and the Balearic Islands in the context of the western Mediterranean," in *Geología de España*, J. A. Vera, Ed., pp. 352–354, SGE-IGME, Madrid, 2004.

[63] S. Martínez-Loriente, V. Sallarès, E. Gràcia, R. Bartolome, J. J. Dañobeitia, and N. Zitellini, "Seismic and gravity constraints on the nature of the basement in the Africa-Eurasia plate boundary: new insights for the geodynamic evolution of the SW Iberian margin," *Journal of Geophysical Research: Solid Earth*, vol. 119, no. 1, pp. 127–149, 2014.

[64] V. Sallarès, A. Gailler, M. A. Gutscher et al., "Seismic evidence for the presence of Jurassic oceanic crust in the central Gulf of Cadiz (SW Iberian margin)," *Earth and Planetary Science Letters*, vol. 311, no. 1-2, pp. 112–123, 2011.

[65] A. Schettino and C. R. Scotese, "Global kinematic constraints to the tectonic history of the Mediterranean region and surrounding areas during the Jurassic and Cretaceous," in *Reconstruction of the Evolution of the Alpine-Himalayan Orogen*, G. Rosenbaum and G. S. Lister, Eds., vol. 7, pp. 147–166, Journal of the Virtual Explorer, 2002.

[66] J. A. Vera, "Evolution of depositional systems in the iberic margin of the Betic Cordillera," *Revista. Sociedad Geologica de España*, vol. 1, pp. 373–391, 1988.

[67] J. A. Vera, "Evolution of south Iberian continental palaeo margin," in *Peritethyan rift/wrench hasins and passive margins Mem*, W. Cavazza, A. H. F. R. Robertson, and P. A. Ziegler, Eds., Mus. Nat. Hist. Nat, París, 1998.

[68] J. A. Vera, J. M. Molina, P. Montero, and F. Bea, "Jurassic guyots on the southern Iberian continental margin: a model of isolated carbonate platforms on volcanic submarine edifices," *Terra Nova*, vol. 9, no. 4, pp. 163–166, 1997.

[69] J. M. Molina, L. O'Dogherty, J. Sandoval, and J. A. Vera, "Jurassic radiolarites in a Tethyan continental margin (Subbetic, southern Spain): palaeobathymetric and biostratigraphic considerations," *Palaeogeography, Palaeoclimatology, Palaeoecology*, vol. 150, no. 3-4, pp. 309–330, 1999.

[70] J. M. Molina and J. A. Vera, "The Milanos Fm in the middle Subbetic (upper Jurassic): definition and description," *Geogaceta*, vol. 20, pp. 29–42, 1996.

[71] J. A. Vera and J. M. Molina, "Shallowing-upward cycles in pelagic troughs (upper Jurassic, Subbetic, southern Spain)," *Sedimentary Geology*, vol. 119, no. 1-2, pp. 103–121, 1998.

[72] J. M. Molina, "Resedimented carbonate and volcanic rocks in the Berriasian-Hauterivianof the Subbetic (Alamedilla, Betic Cordillera, southern Spain)," *Cretaceous Research*, vol. 29, pp. 781–789, 1996.

[73] M. C. Comas, P. Fenoll Hach-Alí, A. López-Galindo, and M. Ortega-Huertas, "Turbiditic pelites and hemipelagic pelites in the Fardes formation (Albian-Upper Cretaceous, Cordilleras Béticas)," *Cuadernos Geología Ibérica*, vol. 8, pp. 483–498, 1982.

[74] J. M. Molina, J. A. Vera, and G. de Gea, "Santonian submarine volcanism in the Subbetic: nannofossils dating and interpretation (Capas Rojas formation, Alamedilla, Granada)," *Estudios Geológicos*, vol. 54, no. 5-6, pp. 191–197, 1998.

[75] P. A. Baedecker, *Methods for geological analysis. US Geological Survey Bulletin*, U.S Geological Survey Bulletin, 1987.

[76] F. Bea, P. Montero, A. Stroh, and J. Baasner, "Microanalysis of minerals by an excimer UV-LA-ICP-MS system," *Chemical Geology*, vol. 133, no. 1-4, pp. 145–156, 1996.

[77] D. Morata, *Petrology and geochemistry of the ophites in the Betic external zones. Thesis Doctoral*, Universidad de Granada, 1993.

[78] E. Puga, M. Portugal, A. Diaz de Federico, G. M. Bargossi, and L. Morten, "The evolution of the magmatism in the external zones of the Betic Cordilleras during the Mesozoic," *Geodinamica Acta*, vol. 3, no. 4, pp. 253–266, 1989.

[79] A. Pérez-López, A. Cambeses, F. Pérez-Valera, and A. E. Götz, "Rhaetian tectono-magmatic evolution of the Central Atlantic Magmatic Province volcanism in the Betic Cordillera, South Iberia," *Lithos*, vol. 396-397, p. 106230, 2021.

[80] J.-L. Bodinier, L. Morten, E. Puga, and A. Diaz de Federico, "Geochemistry of metabasites from the Nevado-Filabride complex, Betic Cordilleras, Spain: relics of a dismembered ophiolitic sequence," *Lithos*, vol. 20, no. 3, pp. 235–245, 1987.

[81] M. T. Gómez-Pugnaire, P. Ulmer, and V. López-Sánchez-Vizcaíno, "Petrogenesis of the mafic igneous rocks of the Betic Cordilleras: a field, petrological and geochemical study," *Contributions to Mineralogy and Petrology*, vol. 139, no. 4, pp. 436–457, 2000.

[82] E. Saccani, K. Allahyari, L. Beccaluva, and G. Bianchini, "Geochemistry and petrology of the Kermanshah ophiolites (Iran): Implication for the interaction between passive rifting, oceanic accretion, and OIB-type components in the Southern Neo-Tethys Ocean," *Gondwana Research*, vol. 24, no. 1, pp. 392–411, 2013.

[83] E. Saccani, K. Allahyari, and B. Rahimzadeh, "Petrology and geochemistry of mafic magmatic rocks from the Sarve-Abad ophiolites (Kurdistan region, Iran): Evidence for interaction between MORB- type asthenosphere and OIB-type components in the southern Neo-Tethys Ocean," *Tectonophysics*, vol. 621, pp. 132–147, 2014.

[84] D. L. Whitney and B. W. Evans, "Abbreviations for names of rock-forming minerals," *American Mineralogist*, vol. 95, no. 1, pp. 185–187, 2010.

[85] M. J. Le Bas, "IUGS reclassification of the high-Mg and picritic volcanic rocks," *Journal of Petrology*, vol. 41, no. 10, pp. 1467–1470, 2000.

[86] H. Furnes, B. Robins, and M. J. de Wit, "Geochemistry and petrology of lavas in the upper Onverwacht suite, Barberton Mountain Land, South Africa," *South African Journal of Geology*, vol. 115, no. 2, pp. 171–210, 2012.

[87] A. Hofmann and A. H. Wilson, "Silicified basalts, bedded cherts and other sea floor alteration phenomena of the 3.4 Ga Nondweni greenstone belt, South Africa," in *Earth's Oldest Rocks*, M. J. Kranendonk, R. H. Smithies, and V. C. Bennett, Eds., vol. 15 of Developments in Precambrian Geology, pp. 571–605, Elsevier, Amsterdam, 2007.

[88] P. Koutsovitis, A. Magganas, T. Ntaflos, N. Koukouzas, A. E. Rassios, and K. Soukis, "Petrogenetic constraints on the origin and formation of the Hellenic Triassic rift-related lavas," *Lithos*, vol. 368-369, p. 105604, 2020.

[89] J. A. Pearce, "immobile Element fingerprinting of ophiolites," *Elements*, vol. 10, no. 2, pp. 101–108, 2014.

[90] J. A. Pearce, "Trace element characteristics of lavas from destructive plate boundaries," in *Andesites*, R. S. Thorpe, Ed., pp. 525–548, Wiley and Sons, New York, 1982.

[91] S.-S. Sun and W. F. McDonough, "Chemical and isotopic-systematics of oceanic basalts: implications formantle composition and processes," in *Magmatism in the ocean basins*, A. D. Saunders and M. J. Norry, Eds., vol. 42, pp. 313–346, Geol. Soc. London, SP, 1989.

[92] J.-G. Schilling, M. Zajac, R. Evans et al., "Petrologic and geochemical variations along the mid-Atlantic ridge from 29 degrees N to 73 degrees N," *American Journal of Science*, vol. 283, no. 6, pp. 510–586, 1983.

[93] E. Saccani, "A new method of discriminating different types of post-Archean ophiolitic basalts and their tectonic significance using Th-Nb and Ce-Dy-Yb systematics," *Geoscience Frontiers*, vol. 6, no. 4, pp. 481–501, 2015.

[94] J. A. Pearce, "Geochemical fingerprinting of oceanic basalts with applications to ophiolite classification and the search for Archean oceanic crust," *Lithos*, vol. 100, no. 1-4, pp. 14–48, 2008.

[95] A. Pedrera, J. García-Senz, C. Peropadre et al., "The Getxo crustal-scale cross-section: testing tectonic models in the Bay of Biscay-Pyrenean rift system," *Earth Science Reviews*, vol. 212, p. 103429, 2021.

[96] J. A. Baker, M. A. Menzies, M. F. Thirlwall, and C. G. MacPherson, "Petrogenesis of Quaternary intraplate volcanism, Sana'a, Yemen: implications for Plume-Lithosphere interaction and polybaric melt hybridization," *Journal of Petrology*, vol. 38, no. 10, pp. 1359–1390, 1997.

[97] S. Brune, C. Heine, M. Pérez-Gussinyé, and S. V. Sobolev, "Rift migration explains continental margin asymmetry and crustal hyper- extension," *Nature Communications*, vol. 5, no. 1, p. 4014, 2014.

[98] M. Pérez-Gussinyé, "A tectonic model for hyperextension at magma-poor rifted margins: an example from the West Iberia-Newfoundland conjugate margins," *Geological Society, London, Special Publications*, vol. 369, no. 1, pp. 403–427, 2013.

[99] C. R. Ranero and M. Pérez-Gussinyé, "Sequential faulting explains the asymmetry and extension discrepancy of conjugate margins," *Nature*, vol. 468, no. 7321, pp. 294–299, 2010.

[100] J.-P. Brun and M. O. Beslier, "Mantle exhumation at passive margins," *Earth and Planetary Science Letters*, vol. 142, no. 1-2, pp. 161–173, 1996.

[101] L. L. Lavier and G. Manatschal, "A mechanism to thin the continental lithosphere at magma-poor margins," *Nature*, vol. 440, no. 7082, pp. 324–328, 2006.

[102] I. Socias and J. Mezcua, *Map of Magnetic Anomalies in the Iberian Peninsula*, Instituto Geografico Nacional, 2002.

[103] C. Annen and R. S. J. Sparks, "Effects of repetitive emplacement of basaltic intrusions on thermal evolution and melt generation in the crust," *Earth and Planetary Science Letters*, vol. 203, no. 3-4, pp. 937–955, 2002.

[104] C. Annen, B. Scaillet, and R. S. J. Sparks, "Thermal constraints on the emplacement rate of a large intrusive complex: the Manaslu leucogranite, Nepal Himalaya," *Journal of Petrology*, vol. 47, no. 1, pp. 71–95, 2006.

[105] J. García Serrano, C. Villaseca, and C. Pérez-Soba, "Depleted lherzolite xenoliths from the leucititic Morron de Villamayor volcano (Calatrava volcanic field, Spain)," *Lithos*, vol. 380-381, p. 105830, 2021.

[106] C. Villaseca, J. García Serrano, and C. Pérez-Soba, "Subduction-related metasomatism in the lithospheric mantle beneath the Calatrava volcanic field (central Spain): constraints from lherzolite xenoliths of the Cerro Gordo volcano," *International Geology Review*, pp. 1–20, 2020.

[107] G. M. Yaxley, "Experimental study of the phase and melting relations of homogeneous basalt + peridotite mixtures and implications for the petrogenesis of flood basalts," *Contributions to Mineralogy and Petrology*, vol. 139, no. 3, pp. 326–338, 2000.

[108] A. Stracke, V. J. M. Salters, and K. W. W. Sims, "Assessing the presence of garnet-pyroxenite in the mantle sources of basalts through combined hafnium-neodymium-thorium isotope systematics," *Geochemistry, Geophysics, Geosystems*, vol. 1, no. 12, 2000.

[109] M. M. Hirschmann and E. M. Stolper, "A possible role for garnet pyroxenite in the origin of the "garnet signature" in MORB," *Contributions to Mineralogy and Petrology*, vol. 124, no. 2, pp. 185–208, 1996.

[110] M. M. Hirschmann, T. Kogiso, M. B. Baker, and E. M. Stolper, "Alkalic magmas generated by partial melting of garnet pyroxenite," *Geology*, vol. 31, no. 6, pp. 481–484, 2003.

[111] S. Lambart, M. B. Baker, and E. M. Stolper, "The role of pyroxenite in basalt genesis: melt-PX, a melting parameterization for mantle pyroxenites between 0.9 and 5 GPa," *Journal of Geophysical Research: Solid Earth*, vol. 121, no. 8, pp. 5708–5735, 2016.

[112] A. K. Matzen, B. J. Wood, M. B. Baker, and E. M. Stolper, "The roles of pyroxenite and peridotite in the mantle sources of oceanic basalts," *Nature Geoscience*, vol. 10, no. 7, pp. 530–535, 2017.

[113] O. Sigmarsson, S. Carn, and J. C. Carracedo, "Systematics of U-series nuclides in primitive lavas from the 1730-36 eruption on Lanzarote, Canary Islands, and implications for the role of garnet pyroxenites during oceanic basalt formations," *Earth and Planetary Science Letters*, vol. 162, no. 1-4, pp. 137–151, 1998.

[114] J. R. Martínez-Catalán, "The central Iberian arc, an orocline centered in the Iberian Massif and some implications for the Variscan belt," *International Journal of Earth Sciences*, vol. 101, no. 5, pp. 1299–1314, 2012.

[115] P. Hooper, J. Rehacek, and G. Morris, "Data report: major and trace element composition, strontium, neodymium, and oxygen isotope ratios, and mineral compositions of samples," in *Proc. ODP*, H. C. Larsen, Ed., vol. 163, pp. 113–117, Science Results, 1999.

[116] A. Gale, C. A. Dalton, C. H. Langmuir, Y. Su, and J. G. Schilling, "The mean composition of ocean ridge basalts," *Geochemistry, Geophysics, Geosystems*, vol. 14, no. 3, pp. 489–518, 2013.